ALMA MATER STUDIORUM - UNIVERSITY OF BOLOGNA

SCHOOL OF ENGINEERING AND ARCHITECTURE

DEPARTMENT OF INDUSTRIAL ENGINEERING (DIN)

MASTER DEGREE IN MECHANICAL ENGINEERING

DISSERTATION

in
COMPUTATIONAL BIOMECHANICS

ASSESSING MODEL CREDIBILITY OF CT-BASED FINITE ELEMENT MODEL TO PREDICT BONE STRENGTH

CANDIDATE

Ferdinando Simoncelli

SUPERVISOR:
Prof. Marco Viceconti

CO-SUPERVISORS
Prof. Alfredo Liverani
Prof. Luca Cristofolini
Dr. Cristina Curreli

Academic year 2020/21

Session III

Abstract

Osteoporosis is one of the major causes of mortality among the elderly that results in massive costs for both individuals and health-care system. The skeletal disease is characterized by a progressively degradation of the bone tissue microarchitecture and an increased risk of fragility fracture. Nowadays, areal bone mineral density (aBMD) measured by Dual-energy X-ray Absorptiometry (DEXA) is used as diagnostic criteria for osteoporosis. However, this is a moderate predictor of the femur fracture risk and does not capture the effect of some anatomical and physiological properties (e.g., three-dimensional geometry and distribution of the bone density) on the bone strength estimation. Data from past research suggest that most fragility femur fractures occur in patients with aBMD values outside the pathological range and defined as non-osteoporotic. Subject-specific finite element models of bones derived from computed tomography (CT) data are considered better tools to non-invasively assess fracture risk in individual patients. In particular, the Bologna Biomechanical Computed Tomography (BBCT) is an In Silico methodology that uses a subject specific FE model to predicts bone strength in a side fall condition. Different studies demonstrated that the modeling pipeline is able to increase predictive accuracy of osteoporosis detection, and to assist the process of assessing the efficacy of new antiresorptive drugs. However, one critical aspect that must be properly addressed before using the technology in the clinical practice, is the assessment of the model credibility based on accepted verification, validation, and uncertainty quantification (VV&UQ) practices.

The aim of this study was to define and perform verification and uncertainty quantification analyses on the BBCT methodology following the risk-based credibility assessment framework recently proposed in the VV-40 standard by the American Society of Mechanical Engineers (ASME V&V-40 2018). The analyses focused on the main verification tests used in computational solid mechanics: force and moment equilibrium check, mesh convergence analyses, mesh quality metrics study, evaluation of the uncertainties associated to the definition of the boundary conditions and material properties mapping. Results of these analyses showed that the FE model is implemented correctly and accurately solved. The operation that mostly affect the model results is the material properties mapping step.

This work represents an important step that, together with the ongoing clinical validation activities, will contribute to demonstrate the credibility of the BBCT methodology. The VV&UQ plan will be soon submitted as evidence for qualification of the method to a regulatory authority.

Contents

1 Basic concepts and state of the art

This chapter provides a general overview of the main concepts that have to be taken into account for this work. A general overview of the femur anatomy is provided, focusing on the main parts, especially those crucial during hip fractures. Different types of hip fractures are described, considering the principal risk factors and the best surgery pathway for each of them. In the third chapter, the possibility to predict hip fractures using FE models is presented analyzing a novel modelling approach. The last two sections of this chapter regard model credibility assessment concepts and Verification, Validation and Uncertainty Quantification (VV&UQ) of FE models. A general overview of the ASME V&V-40 standard, best practices to perform V&V in orthopedic biomechanics and relevant applications of VV&UQ are finally presented.

1.1 Anatomy of the femur

The femur is the longest and strongest bone in the human body (Driscoll, 2006). It has an approximately cylindrical and rounded forward shaft and an articular head projecting mainly medially on its neck, which is a medial deflection of the proximal shaft. The distal extremity is bigger and has two condyles that articulates with the tibia. Femoral obliquity generally changes between individuals, but is greater in women, reflecting the relatively greater pelvic breadth and shorter femora. Proximally the femur consists of a head, neck, and two trochanters: the greater and the lesser (Fig. 1.1).

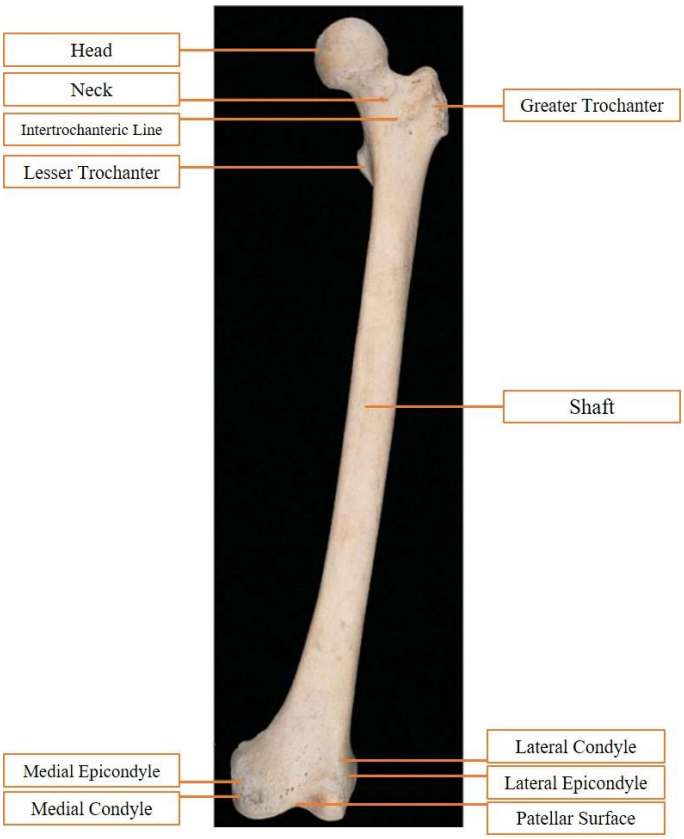

Fig. 1.1 Anatomy of a right femur

1.1.1 Femoral head

The femoral head faces anterosuperomedially to articulate with the acetabulum. The head, which is intracapsular, is spheroidal and is part of the surface of an ovoid. Its smoothness is interrupted posteroinferior to its centre by a small, rough fovea, to which the ligamentum teres attaches (Fig. 1.2).

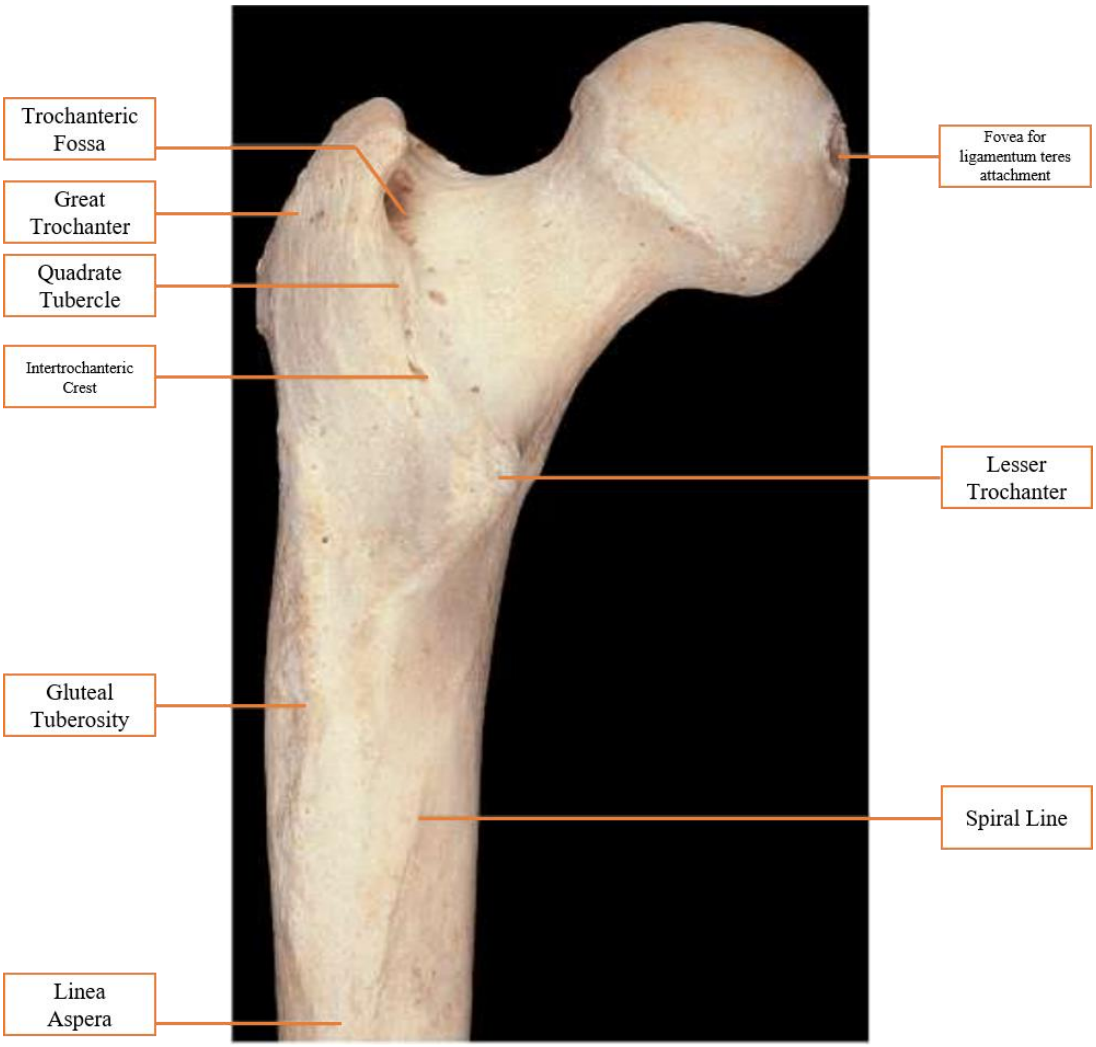

Fig. 1.2 Anatomy of a femoral head

1.1.2 Femoral neck

The femoral neck is around 5 cm long, tightest in its mid part and broadest laterally, and connects the head to the shaft at an angle of inclination around 125°: this allowing the limb to swing clear of the pelvis. The neck also represents a lever for the action of the muscles acting in the hip joint, which are linked to the proximal femur. The neck-shaft angle is widest at birth and decreases until adolescence; it is smaller in females. The neck is laterally rotated with respect to the shaft (angle of anteversion) of 10-15°. The contours of the neck are rounded: the upper surface is almost horizontal and

moderatly concave, the lower is straighter but oblique. On all aspects the neck expands as it approaches the articular surface of the head.

1.1.3 Trochanters

The greater trochanter is large and quadrangular, extruded from the junction of the neck and shaft. Its lateral surface is palpable, especially when the muscles are relaxed. The lesser trochanter is a conical posteromedial projection of the shaft at the posteroinferior aspect of its junction with the neck. It is not palpable. The intertrochanteric line is a prominent ridge at the junction between the anterior surfaces of the neck and shaft. It descends medially from a superomedial tubercle on the anterior aspect of the greater trochanter to a point on the lower edge of the neck, anterior to the lesser trochanter. This line is the lateral limit of the hip joint capsule anteriorly. The intertrochanteric crest, a smooth ridge at the junction of the posterior surface of the neck with the shaft, descends from the posterosuperior angle of the greater trochanter medially down to the lesser trochanter. The gluteal tuberosity may be an elongated depression or a ridge. It may in part be prominent enough to be called a third trochanter.

1.1.4 Shaft

The shaft is encircled by muscles and is impalpable. The shaft is closest centrally, expanding a little proximally, particularly towards its distal end. Its long axis makes an angle of about 10° with the vertical and diverges in a range of about 5- 7° from the long axis of the tibia. The posterolateral surface is boundaried posteriorly by the broad, coarse linea aspera, usually a crest with lateral and medial edges. Its subjacent compact bone is augmented to resist to compressive forces, which are concentrated here by the anterior curvature of the shaft. Nutrient foramina, directed proximally, appear in the linea aspera.

1.1.5 Distal end

The distal end of the femur is widely expanded as a bearing surface for transmission of weight to the tibia. It has two massive condyles, which are partly articular. Anteriorly the condyles unite and continue into the shaft; posteriorly they are disconnected by a deep intercondylar fossa and project beyond the plane of the popliteal surface (Fig. 1.3). The articular surface is a vast area, like an inverted U, for the patella and the tibia. The tibial surface is divided by the intercondylar fossa but is anteriorly continuous with the patellar surface. The tibial surfaces are transversely convex in all directions. It has been suggested that the medial articular surface describes arcs of two circles. Laterally there may only be one arc of fixed curvature with a radius similar to that of the posterior arc of the medial femoral articular surface. These differences are important determinants of knee joint motion.

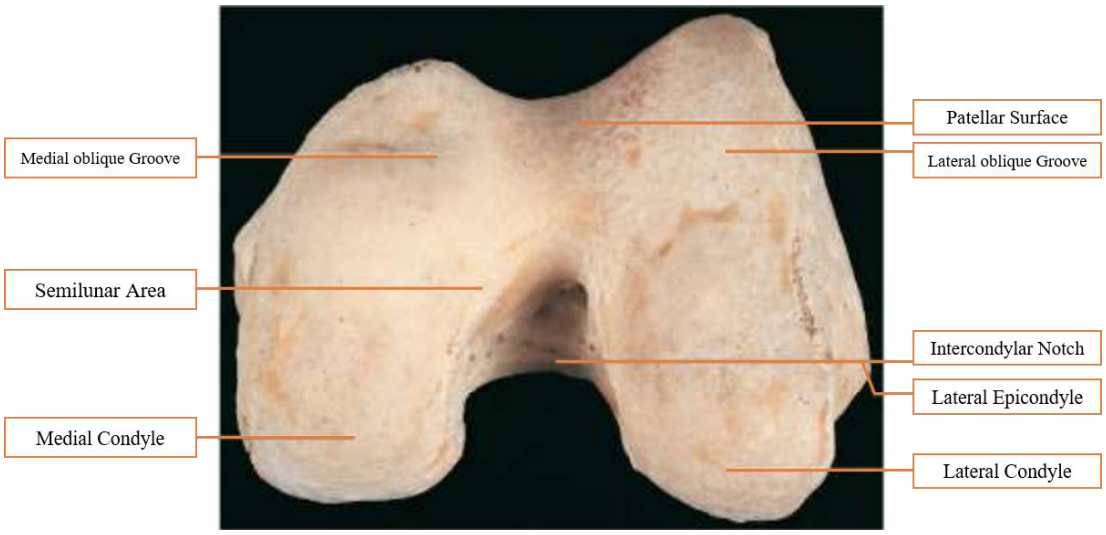

Fig. 1.3 Anatomy of a femoral distal end

1.1.6 Structure

The femoral shaft is a cylinder of compact bone with a wide medullary cavity (Fig. 1.4). Moving proximally and distally the compact wall becomes progressively thinner, and the cavity gradually fills with trabecular bone. The extremities, especially where articular, consist of trabecular bone within a thin frame of compact bone, their trabeculae being disposed along lines of greatest stress. At the proximal end, the main trabeculae form a series of plates orthogonal to the articular surface, converging to a central dense wedge, which is supported by strong trabeculae passing to the sides of the neck, especially along its upper and lower profiles. Force applied to the femoral head is therefore transmitted to the wedge and thence to the junction of the neck and shaft. This junction is reinforced by dense trabeculae extending laterally from the lesser trochanter to the end of the superior aspect of the neck, thus resisting tensile or shearing forces applied to the neck through the head. Tensile and compressive tests indicate that axial trabeculae of the femoral head tolerate much greater stresses than peripheral trabeculae. A smaller bar across the junction of the greater trochanter with the neck and shaft resists shearing produced by muscles attached to it. These two bars are proximal layers of arches between the sides of the shaft and transmit to it forces applied to the proximal end. At the distal end of the femur, trabeculae arise from the entire internal surface of compact bone, going down perpendicular to the articular surface. Proximal to the condyles these are strongest and most accurately perpendicular.

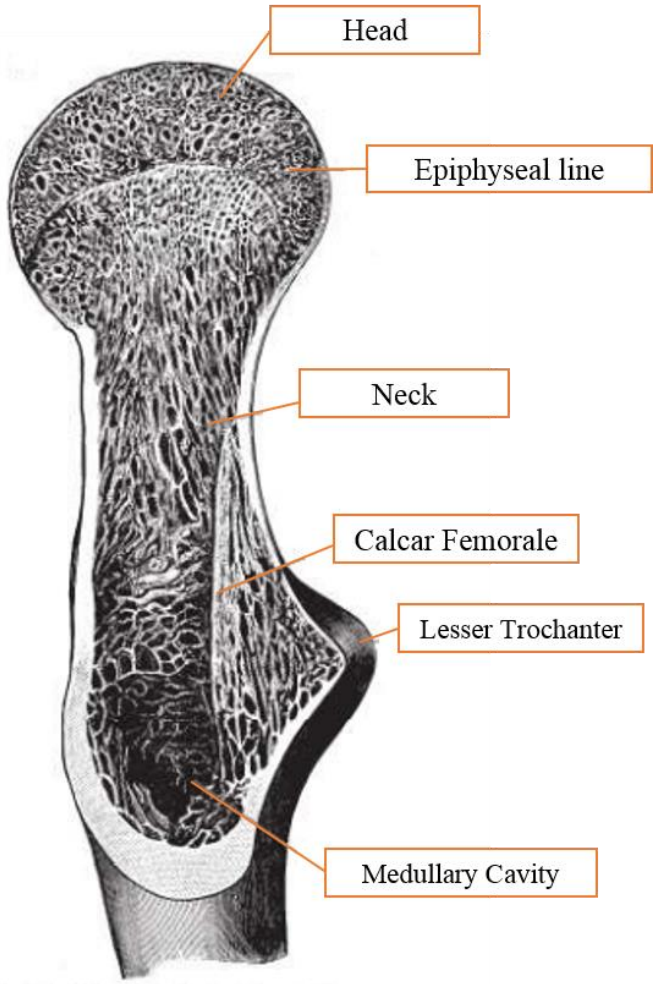

Fig. 1.4 Section of a femoral head

1.2 Osteoporosis and hip fractures

1.2.1 Osteoporosis

Osteoporosis is the most common chronic metabolic bone disease, characterized by reduced bone mass and degradation of the bone tissue framework. Osteoporosis causes increased bone fragility and, therefore, a major risk of fracture. This condition is better defined measuring bone mineral density through non-invasive methods, like Dual-energy X-ray absorptiometry (DXA / DEXA) and Quantitative Computer Tomography (QCT) and comparing these measures to that of a healthy adult. The difference is calculated as a standard deviation and is called T score. A T score of:

- above -1 SD is normal
- between -1 and -2.5 SD shows bone loss and is defined as osteopenia
- below -2.5 shows bone loss and is defined as osteoporosis.

Osteoporosis can be divided in two wide groups: primitive forms and secondary forms.

PRIMITIVE	SECONDARY				
	Endocrine Disorders	**Neoplasia**	**Gastrointestinal**	**Drugs**	**Miscellaneous**
Postmenopausal	Hyperparathyroidism	Multiple Myeloma	Malnutrition	Anticoagulants	Osteogenesis imperfecta
Senile	Hyperthyroidism	Carcinomatosis	Malabsorption	Chemotherapy	Immobilization
Idiopathic	Hypothyroidism		Hepatic Insufficiency	Corticosteroids	Pulmonary Disease
	Hypogonadism		Vitamin C, D deficiencies	Anticonvulsants	Homocystinuria
	Pituitary tumors			Alcohol	Anemia
	Diabetes, type one				

Tab. 1.1 Forms of osteoporosis

Among primitive forms (tab 1.1), the most important and diffused is the postmenopausal, involutive and senile osteoporosis (Gennari and Avioli, 1991). Indeed, starting from the fourth decade of life, both for man and women begins a progressive loss of bone mass (1.5–4% per year). The latter is the resultant of the processes of bone formation and resorption; osteoporosis is a physiological process due to an absolute or relative increase of the deconstruction processes, compared to those of deposition. In general, this phenomenon behaves differently among the sexes: it is slow and constant in the male population and variable for the female one. Indeed, for women this loss process increases quickly between menopause and the age of 70, and then became steady, similarly to the male one. Generally, osteoporosis is treated with drugs that reduce the rate of bone resorption, like bisphosphonates, or rarely that speed up the bone building process. Those latter are typically reserved for people who have very low bone density.
Factors that can contribute to the onset of osteoporosis are genetical, endocrine and bad habits like bad diet, smoke, alcohol abuse and sedentary lifestyle. For postmenopausal women bone loss is primarily due to deficit of estrogen, which causes a higher production of osteoclasts; this can also happen after ovariectomy. Two morphological-functional types of osteoporosis exist: the “high metabolic turnover” and the “low or normal metabolic turnover”, differentiating in the number of osteoclasts and osteoblasts that are higher in the first type.

Osteoporosis is one of the major causes of mortality and health expenditure in the world. Currently, it has been estimated that more than 200 million of women are suffering from osteoporosis worldwide, and that 1 in 3 women over the age of 50 years and 1 in 5 men will experience osteoporotic fractures in their lifetime. In Europe the cost of osteoporosis, including pharmacological intervention, was estimated at € 37 billion in 2010 (“International Osteoporosis Foundation | IOF,” n.d.).
Most common osteoporotic fractures are Colles fractures (in the wrist), vertebral fractures (affecting standing) and hip fractures. The latter is without doubt one of the most dangerous, because may cause deep vein thrombosis, pulmonary embolism and increased mortality. Indeed, 12-36% of patients that had experienced hip fracture dies within a year from the event.

1.2.2 Hip Fractures

A hip fracture is a break that happen in the upper part of the femur (Apple and Hayes, 1993). Most common symptoms are impossibility to walk, pain with movements of the hip, shortening and external rotation of the fractured leg. Imaging studies are usually considered for the diagnosis of hip fractures. Magnetic resonance imaging (MRI) techniques are the most sensitive for the evaluation of fractures, in particular for hidden or nondisplaced fractures. MRI scans can be used immediately after injury and can reveal soft-tissue pathology, such as muscle strains, greater trochanteric bursitis, and pelvic fractures. Plain radiographs may appear normal or inconclusive, and CT scans reveal fractures only when they are displaced.

From 81 to 98% of fractures in elderly occur after a fall, in Italy in 2002 was esteemed that 28.6% of people over 65 falls at least one time in a year, and 43% of them falls more times (Schrøder et al., 1993). Besides osteoporosis, there are other risk factors for hip fractures related to less common metabolic bone diseases like osteogenesis imperfecta, or metastatic cancer in the femur. Moreover, elderly often have motor control issues like low balance and compromised proprioception, that increase the probability to fall. The direction of the fall is also important: elderly tend to fall to the side instead of forward, and the hip strikes the ground first laterally. During a sideways fall, the chances of hip fracture see a 15-fold and 12-fold increase in elderly males and females, respectively (Endo et al., 2005).

There are three broad categories (Fig. 1.5) of hip fractures based on the location of the fracture (Löfman et al., 2002)
- intracapsular fractures, that affect femoral head and femoral neck;
- trochanteric fractures subdivided into intertrochanteric and pertrochanteric;
- subtrochanteric fractures.

Pertrochanteric and intertrochanteric fractures are often considered synonyms because the difference between these types is minor. Femoral head and subtrochanteric fractures represent around 10% of the whole fracture; neck and trochanteric occur in an almost equal number. Although other more detailed classification systems exist, in general fractures are classified as stable and unstable, and the differences between those two will be explained case by case.

Femoral neck fractures

A femoral neck fracture is intracapsular when is within the hip joint and beneath the fibrous joint capsule. The femoral neck is the most common location for a hip fracture, accounting for 45% to 53% of hip fractures.

Stable fractures are nondisplaced and manifest no deformity. To detect them, MRI scanning may be required. Treatment is by operative pinning with three parallel cannulated screws placed adjacent to the femoral neck cortex (Koval and Zuckerman, 1994). Unstable femoral neck fractures are displaced and can be seen on plain radiographs. Displaced fractures in young patients are usually treated with pinning.

Hemi or total joint arthroplasty is often the better option for older patients. In hemiarthroplasty the acetabular cartilage is left intact, and the implant articulates with the acetabulum. During a total joint replacement, the acetabulum is resurfaced and a metal cup with a polyethylene liner is fixed inside.

Trochanteric Fractures

Trochanteric fractures are breaks of the femur between the greater and the lesser trochanters and account for approximately 38% to 50% of all hip fractures. The epidemiology of trochanteric fractures is similar to that of femoral neck fractures.

Stable fractures are those in which the femur is broken into two or three parts. The treatment is with a sliding hip screw coupled to a side plate that is screwed onto the femoral shaft.

Unstable fractures are those in which the femur is broken into four parts or the fracture is of the reverse oblique pattern. Fractures with multiple pieces and fracture lines are termed “comminuted”. The more pieces, the less stable is the fracture pattern. For unstable trochanteric fractures an intramedullary hip screw is indicated. This device combines a sliding hip screw with an intramedullary nail that acts as a metal buttress preventing sliding and providing better fixation in unstable fracture patterns (Baumgaertner et al., 1995).

Subtrochanteric Fractures

Subtrochanteric fractures are located between the lesser trochanter and the femoral isthmus that is in the proximal part of the femoral shaft. They are less common than femoral neck and trochanteric fractures, accounting for approximately 5% to 15 % of hip fractures.

Subtrochanteric fractures are less stable than the other two types of hip fractures and, consequently, more difficult to fix. A subtrochanteric fracture is treated with an intramedullary hip screw. No lateral buttress exists in a subtrochanteric fracture and, therefore, sliding hip screws with side plates provide poor fixation.

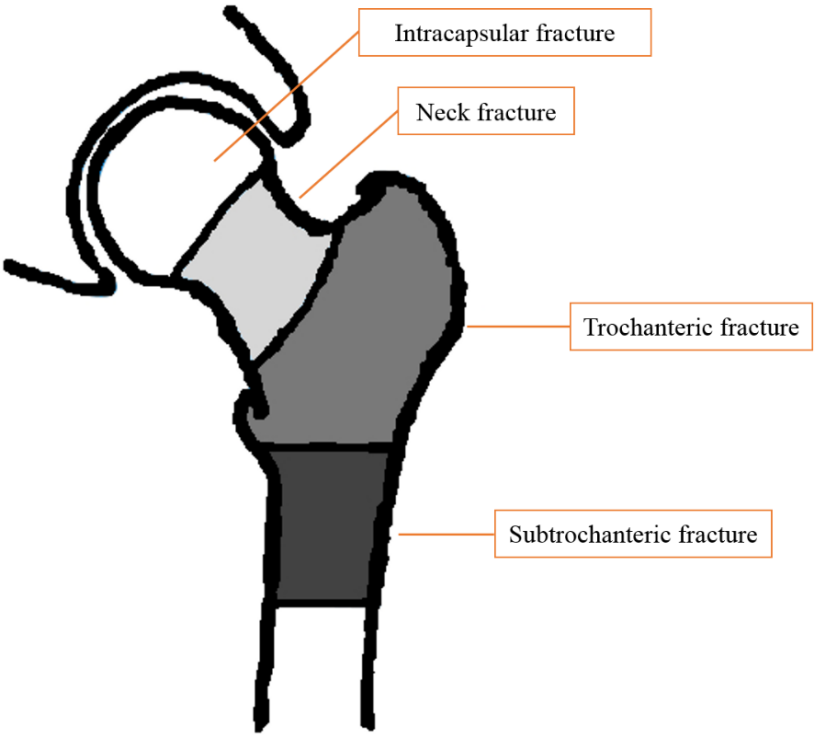

Fig. 1.5 Types of hip fracture

1.3 Finite Element Models to predict hip fractures

As said before, nowadays the risk of hip fractures is assessed with DXA exam. After DXA examination, statistically 70% of visited patients receive no pharmacologically treatment, and a half experience a hip fracture. The same rate for the remaining treated 30%. Those data suggest firstly that drugs have no significant effect, and that 50% of fractures occur in non-osteoporotic patients. Over the years different methods to predict hip fractures have been proposed, like statistical regression models (e.g., FRAX), mechanistic models and so on. The latter rely on the fact that fracture risk depends on the bone strength, which is the minimum load required to fracture a bone from a given impact orientation. Subject-specific finite element models of bones derived from computed tomography (CT) data are tools to non-invasively assess the stress-state and fracture risk of bones in individual patients, basing on the bone strength and fall severity (and ageing-related changes as well).

In this section, a general overview of the main FE pipelines available in literature for computing the hip fracture risk is presented. Five different Biomechanical Computed Tomography (BCT) methods are described and named based on the city where the computational workflow have been developed. Main features of the different techniques are then summarised and compared.

1.3.1 CBCT (California Biomechanical Computed Tomography)

In (Amin et al., 2011) and (Orwoll et al., 2009), the pelvic region was scanned from just above the femoral head to 3.5 cm below the lesser trochanter at settings of 80 kVp, 280 mA and in-plane pixel dimension of 0.74 x 0.74.

To estimate proximal femur Strength, the QCT images were processed and converted into FE models using 1.5-mm-sided, cube-shaped, eight-nodes brick elements through a custom code (O.N. Diagnostics, Berkeley, CA, USA). The local isotropic material properties (different between both cortical/trabecular bone and tension/compression load) were assigned to all elements by converting the HU values from CT scan using empirical relations (Morgan et al., 2003) that accurately represent the experimental evidence. Each subject-specific FEA model then was virtually loaded to failure in simulation of an unprotected sideways fall with impact on the greater trochanter, using an in-house FE solver. Nonlinear analyses were used in these simulations, assuming a modified von Mises–type failure criterion for the bone tissue. In this pipeline, strength was calculated from the resulting nonlinear force–deformation curve as the force at 4% deformation of the femoral head with respect to the greater trochanter (Correlation with laboratory experimental data obtained using 76 cadavers loaded in sideways fall configuration: $R^2 = 0.78$).
To determine the load-to-strength ratio at the proximal femur, estimated loads experienced in a sideways fall were related to the bone strength derived from the FEA models. The calculated AUC (area under curve) was 0.84 for women and 0.77 for men.

1.3.2 ZBCT (Zürich Biomechanical Computed Tomography)

In the study conducted by (Enns-Bray et al., 2019) CT scans were obtained using 120 kVp, tube current exposure of 150 mAs and 1.0 mm slice thickness. On the impact side, proximal femur only was considered, and the volume was meshed with 10-node tetrahedral elements with a target length of 3 mm. Distal femur and tibial geometry were estimated using a statistical shape model and modelled using linear elastic shell elements with length of 5 mm, thickness of 6 mm and modulus of 22 GPa. Bone tissue material properties were assigned converting CT units to elastic modulus through validated equations also used in the CBCT. This pipeline also accounts for pelvis, contralateral femur and soft tissues. The bone geometry was meshed using the same methodology of the impact femur, using 4-node tetrahedral elements. The soft tissues were meshed with a target length of 10 mm, decreasing in proximity of bone to 3mm and variable material properties.

To estimate femur strength, a sideway fall with one degree of freedom (DoF) was simulated. The rigid floor was modelled with $0.5m^2$ surface, and the tangential velocity at impact point was settled to 3 m/s. Femoral strength was evaluated as the maximum resultant force passing through the femoral neck during loading. The calculated AUC was 0.85.

1.3.3 TBCT (Torino Biomechanical Computed Tomography)

In the study conducted by (Aldieri et al., 2018) the CT images were segmented through a semi-automatic procedure. Then, FE mesh with 10-node tetrahedra with 1.2 mm edge size was built. At all elements, linear isotropic material properties were assigned using the same laws considered in the CBCT pipeline.
A sideway impact was simulated via a mass-spring-damper system, in which the mass is specific for each patient and the spring-damper values were kept fixed. The peak value of the load was applied on the trochanteric surface, while the femur head nodes were bounded to the ground using spring elements with k = 10.000 N/mm. Distal nodes were connected to a spherical joint placed 0.1 m distally by means of link elements. The failure criteria chosen by this study was strain-based. Risk of fracture (RF) was evaluated as the ratio between ε_{max} and ε_{lim}, where ε_{lim} was the compressive (or tensile) limit value. Based on the RF value, three levels of risk were defined from low to high. This study did not refer to any further analysis to evaluate absolute fracture risk.

1.3.4 T-ABCT (Tel-Aviv Biomechanical Computed Tomography)

In the studies conducted by (Sternheim et al., 2018) the CT scans were obtained using the following parameters: 140 kVp, 250 mA, 0.75 mm slice thickness, pixel size 0.78mm. Femur geometry was then meshed in tetrahedral elements using a p-FE, in other words a model based on polynomial shape functions with a lever varying from 1 to 5. Advantages of this type of mesh can be found here (Yosibash et al., 2007). Inhomogeneous isotropic material properties were assigned to elements converting HU in Elastic Module. The peculiarity of this conversion is the use of phantom-less calibration and different equations for trabecular and cortical bone. Eventually, a moving average of properties was computed using a cubical shape varying on the region. To evaluate bone strength a strain based criterion was used. Those studies did not refer to any further analysis to evaluate femur fracture risk.

1.3.5 BBCT (Bologna Biomechanical Computed Tomography)

The BBCT pipeline will be described in detail in Chapter 2. The main workflow was obtained based on the studies conducted by (Qasim et al., 2016) and (Altai et al., 2019) where a novel multiscale modelling approach is proposed, combining different space-time scales and variability of impact forces. CT scans of the femur were performed at 120 KVp, variable tube current and 0.625 mm slice thickness. Once the geometry was obtained, femur was meshed using 10-node tetrahedral elements with 3 mm edge size. Element Elastic Module was evaluated according to (Schileo et al., 2008) converting HU values through the in-house made software BoneMat®. Based on the location of specific anatomical landmarks, a reference system was then defined. Several falling scenarios were simulated varying both load direction and point of force application. FE Strength was evaluated following a maximum principal strain-based criterion. In short, the FE strength is the load that causes the principal strain to be greater than the limit value (0.73% tensile limit strain, 1.04 % compressive) in the femoral external surface.
Two further models were implemented accounting for body-floor impact and ground-skeleton force transfer. The calculated AUC was 0.84.

		CBCT (Orwoll et al., 2009)	ZBCT (Enns-Bray et al., 2019)	TBCT (Aldieri et al., 2018)	T-ABCT (Stemheim et al., 2018)	BBCT (Qasim et al., 2016)
CT scan	Peak Kilovoltage	80 kVp	120 kVp	-	140 kVp	120 KVp
	x-ray tube current	280 mA	150 mAs	-	250 mA	-
	Slice thickness	-	1.0 mm	-	0.75 mm	0.625 mm
Mesh	Max edge size	1.5 mm	3mm	1.2mm	-	3 mm
	Element type	8 nodes brick	10 nodes tetrahedra	10 nodes tetrahedra	tetrahedra	10 nodes tetrahedra
	Software	-	ANSA (v17.0, BETA CAE Systems, Thessaloniki, Greece).	-	-	(ICEM CFD 14.0, Ansys Inc., PA,USA)
Mat. Properties	Type	local isotropic	local isotropic	local isotropic	local isotropic	local isotropic
	Equations	-	$\rho_{ash} = \frac{\frac{mgHA}{1000} + 0.09}{1.14}$		$\rho_{ash} = 0.877(1.21\rho_{K2HPO4}) + 0.08$	$\rho_{ash} = 0.877\rho_{QCT} + 0.079$
		-	$\rho_{app} = \rho_{ash}/0.6$		$\begin{cases} E_{cort} = 10{,}200\rho_{ash}^{2.01} \\ E_{trab} = 2{,}398 \\ E_{trab} = 33900\rho_{ash}^{2.2} \end{cases}$	$\rho_{app} = \rho_{ash}/0.6$
		$E = 6{,}850\rho_{app}^{1.49}$	$E = 6{,}850\rho_{app}^{1.49}$	$E = 6{,}850\rho_{app}^{1.49}$		$E = 6{,}850\rho_{app}^{1.49}$
Simulations	Fall type	sideways fall	sideways fall	sideways fall	sideways fall	sideways fall
	Software	Custom code	LS-Dyna v11.0, LS-Dyna, Livermore, CA, USA	Abaqus (v13, Simulia,Dassault Systemes, Providence, RI)	StressCheck®	(Ansys Inc., PA, USA)
Failure Criteria		Stress-based	Strain-based	Strain-based	Strain-based	Strain-based
AUC		0.84, 0.77	0.85	-	-	0.84

Tab. 1.2 Main features of the different FE models used to predict the risk of hip fracture. A dash is placed where no information was found.

1.4 The V&V40 standards

During the whole PLC (Product Life Cycle) of medical devices, computational models are massively used in order to ensure performance, safety and correct functionality of the product, but also to support development and maintenance. Establishing model credibility for medical devices design is fundamental because patients and healthcare providers may be subjected to risk that can result in adverse outcome both for the first (potential harm) and the latter (financial loss or increased time to market) (Fig. 1.6). Those factors have led the American Society of Mechanical Engineers (ASME) to release the new standard V&V-40 2018 (ASME, 2018) to assess model credibility through verification and validation activities (V&V). Verification is the "confirmation by examination and provision of objective evidence that specified requirements have been fulfilled" and validation is the "confirmation by examination and provision of objective evidence that the particular requirements for a specific intended use can be consistently fulfilled." ("CFR - Code of Federal Regulations Title 21")

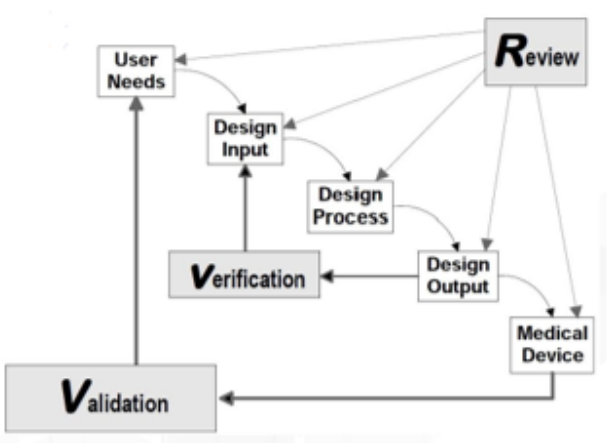

Fig. 1.6 V&V in medical device development

The Standard V&V-40 provides a framework to evaluate a risk-informed credibility assessment of a computational model and choose a correct level of credibility to inform a decision. Indeed, the credibility level must be proportionate to the degree to which the computational model is relied on.

The risk-informed credibility assessment framework begins with identifying a question of interest (QOI), which describes the specific question, decision, or concern that is being addressed. The following are the steps of the risk-informed credibility assessment framework (Fig. 1.7)

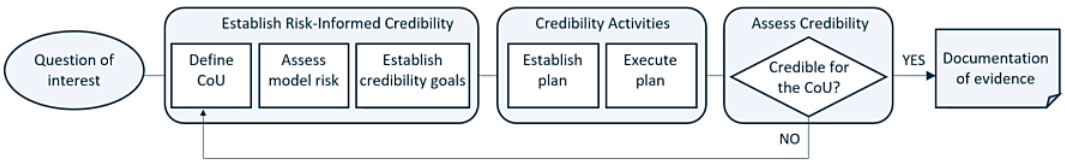

Fig. 1.7 Process diagram of the risk informed credibility assessment framework

1.4.1 Context of Use

The context of use (COU) is a statement that describes the specific role and purpose of the computational model used to inform that decision. In other words, the COU is the intended use of the model to solve the question of interest.

1.4.2 Model Risk

"Model risk is the possibility that the model may lead to a false/incorrect conclusion about device performance, resulting in adverse outcomes like patient harm" (ASME, 2018). To assess model risk, two independent factors must be taken into account: model influence and decision consequence.

I. Model Influence

Model influence is the contribution of the computational model to the decision relative to other available evidence. It is possible to set a three-level gradation of model influence (low, medium and high).

II. Decision Consequence

"Decision consequence is the significance of an adverse outcome resulting from an incorrect decision" (ASME, 2018). It is possible to set a three-level gradation of decision consequence (low, medium and high).

Since the credibility of the computational model should be commensurate with model risk, the model risk analysis drives the section of V&V activities and goals for the credibility factors.

The following figure (Fig. 1.8) shows which relationship subsist between model risk depending on model influence (x-axis) and decision consequence (y-axis), which are independent one to each other. An increase in one of the two variables leads to an increase in the overall model risk.

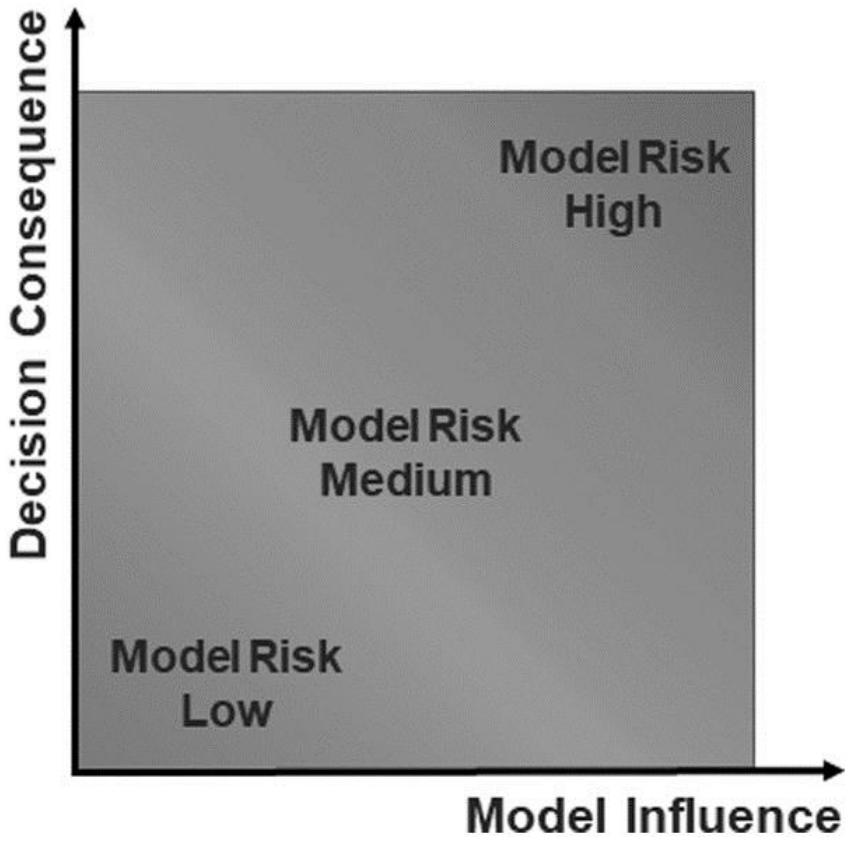

Fig. 1.8 Schematic representation of how model influence and decision consequence determine model risk

1.4.3 Model Credibility

"Model credibility is the trust, established through the collection of evidence, in the predictive capability of a computational model for a specific COU" (ASME, 2018). The process to establish credibility consist in V&V evidence collection, which includes the following activities:

- Verification (code and calculation)
- Validation (computational model, comparator and assessment)
- Applicability

Credibility factors are used to determine the rigor needed for each step in the V&V process and to demonstrate applicability (Fig. 1.9).

A gradation of activities representing rising levels of investigation into each factor is associated with each credibility factor. Determine goals for each credibility factor is fundamental during the V&V activities and applicability assessment, to have the whole model credibility proportionate with the model risk. It is possible to assign numerical values for each credibility factor gradation. A PIRT (phenomena identification and ranking table) is a useful tool providing the logic behind the goal assessment for each credibility factor.

Activities		Credibility Factors
Verification	Code	Software Quality Assurance
		Numerical Code Verification
	Calculation	Discretization Error
		Numerical Solver Error
		Use Error
Validation	Computational Model	Model Form
		Model Inputs
	Comparator	Test Samples
		Test Conditions
	Assessment	Equivalency of Input Parameters
		Output Comparison
Applicability		Relevance of the Validation Activities to the COU
		Relevance of the Quantities of Interest

Fig. 1.9 Verification, validation and applicability activities and their associated credibility factors

1.4.3.1 **Verification**

The aim of the verification activity is to make sure that the hidden mathematical model is rightly implemented and solved. Verification itself is made up of two activities: code verification and calculation verification.

I. Code Verification

By means of code verification, errors in the source code and numerical algorithms of the computational software can be found and removed. The activity of code verification encompasses:

- SQA (Software Quality Assurance).
  This activity assures the correct functionality and result repeatability of the software.
- NCV (Numerical Code Verification).
  This activity proves the correct implementation and functioning of the numerical algorithms, investigating on spatial and temporal convergence rates, even in presence of discontinuities. Generally, NCV is attended by comparing numerical solution to exact benchmark solutions.

II. Calculation Verification

"Calculation verification helps to ensure that the spatial and temporal convergence behaviour of the solution of the computational model is analysed and quantified by refining the discretization parameters and solver convergence tolerances" (ASME, 2018). The activity of calculation verification encompasses:

- Discretization Error: arise solving the computational problem at a finite number of spatial and/or temporal grid points
- Numerical Solver Error: originates from the numerical solution based on the selection of solver parameters (e.g. convergence tolerance)
- Use Error: the errors accumulated in the simulation result by the practitioner.

For FE models used in computational solid mechanics, it is advantageous to subdivide this activity in three parts: general calculation verification, mesh convergence analysis and mesh quality assessment.

a. *General calculation verification*. Those checks regard force and displacement residuum and assure that force application equals force reaction (action = reaction).

b. *Mesh convergence analysis*. The aim is to ensure sufficient discretization and to minimize the influence of the mesh edge size on the results. This is because, according to Patch Test, increasing mesh density both global and local outcome parameters converge. Local outcome parameters are generally the study's results at defined points of interest. In addition, convergence of the local outcome parameters is not a consequence of the convergence of global outcome parameters. For the first ones, additional global mesh refinement must be considered. The following three steps are necessary to compute mesh convergence for a FE model:
   - Define an initial mesh size based on the component geometry.
   - Refine the mesh at least three times rising the degrees of freedom with a ratio of at least 1:1.5.
   - For the result parameters, a convergent behavior should be observed. Typical values for acceptable convergence criterion, are in the range of 1–5%. Mesh refinement steps are repeated until this criterion is met for all outcome parameters.

   The mesh applicable for the FEA is the one for which the quantity of interest falls in the range above after the last refinement step. If the quantity of interest does not show a convergent behavior, more data points and thus a higher mesh density is required. If just the overall deformation but not one (or more) local outcome parameter converges within Step 3, a local mesh refinement should be considered.

c. *Mesh quality assessment:* mesh quality (e.g., shape, aspect ratio, element Jacobians) must be checked and documented.

1.4.3.2 **Validation**

"Validation is the process of assessing the degree to which the computational model is an appropriate representation of the reality of interest" (ASME, 2018). As a consequence, validation aims to confirm the calculated results experimentally and to check the predictive capacity of the model by comparing the predictions of the model with the results obtained from the comparator (in vitro or in vivo). A comparator is an experiment that provides data against which simulation result are evaluated. Also results from literature derived by investigating similar cases in silico and experimentally can be compared with the results obtained with the model. In a final report, justifications as to why the literature data is suitable for validation should be added, assigning a value of credibility. Once the outputs from V&V activities are collected and compared, the accuracy of the simulation outcome can be assessed.

1.4.3.3 **Applicability of the Validation Activities to the COU**

Often, the quantities of interest (QOIs) for the COU are not directly measurable: this could lead to a mismatch between the measured QOIs of the validation activities and those for the COU. Applicability is the relevance of validation activities to support the use of the computational model for a COU. To assess the applicability of the validation activities, validation points can be graphed in a multi-axes diagram (Fig. 1.10), one for every computational model parameter. The greatest level of applicability occurs where the COU overlaps one or more validation points. Two factors determine the applicability of the validation activities:

- Relevance of the QOIs: establishes the similarity between the QOIs from the validation activities and those from the COU.
- Relevance of the validation activities to the COU: summarizes the relative proximity of the COU to the validation points.

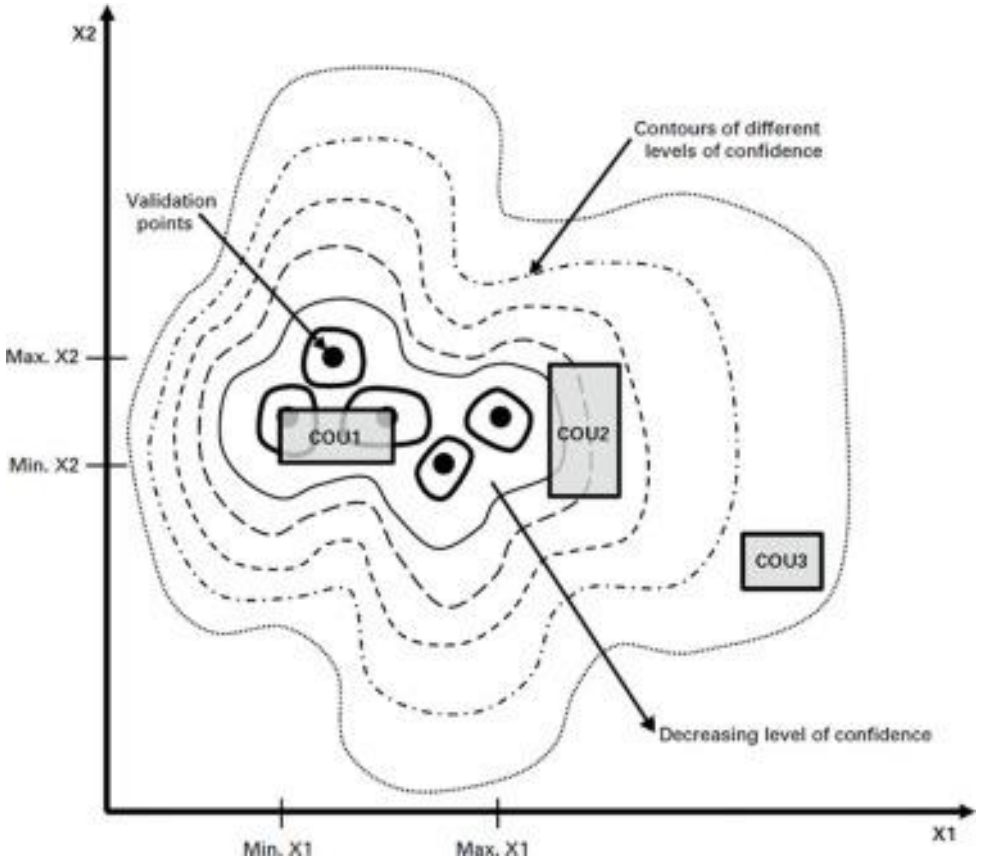

Fig. 1.10 Example of three COUs relative to the validation points for a two-parameter (X1, X2) computational model

1.4.4 Credibility Assessment

The appropriate activities and acceptable results for each credibility factor are defined. This activity relies on the relationship between model influence and decision consequence to the overall model risk, and the translation of that risk into the credibility goals. Done that, the credibility of the computational model for the COU is assessed reviewing the results of V&V. It is possible that the credibility goals don't respect the initial expected outcomes. In those cases, additional credibility activities can be conducted, reduce the influence of the computational model, or modify the COU to lower model risk. Eventually, the credibility activities and evidence supporting the credibility of the computational model should be accurately supplied.

1.5 Relevant application of the model credibility assessment procedure

In this chapter, few applications of the risk-based credibility assessment according to the V&V40 standard are presented. Only articles inherent orthopedic solid biomechanics are considered.

1.5.1 Contact mechanics in total ankle arthroplasty (TAA)

In the study presented by (Dharia et al., 2020), a computational model to predict contact area between tibial bearing and talar component was developed. An experimental test was conducted and data from this latter were compared with those from the model to assess credibility following the guidelines of standard ASME V&V-40 2018.

- QOI: Does the metal-polyethylene implant resist to wear and damages?
- COU: The purpose of the computational model is to evaluate contact area of TAA designs

Model influence is HIGH, since the outputs from the computational model are a significant factor in the decision, so as for the decision consequence, because an incorrect decision of the implant size could lead to implant failure or loosening.

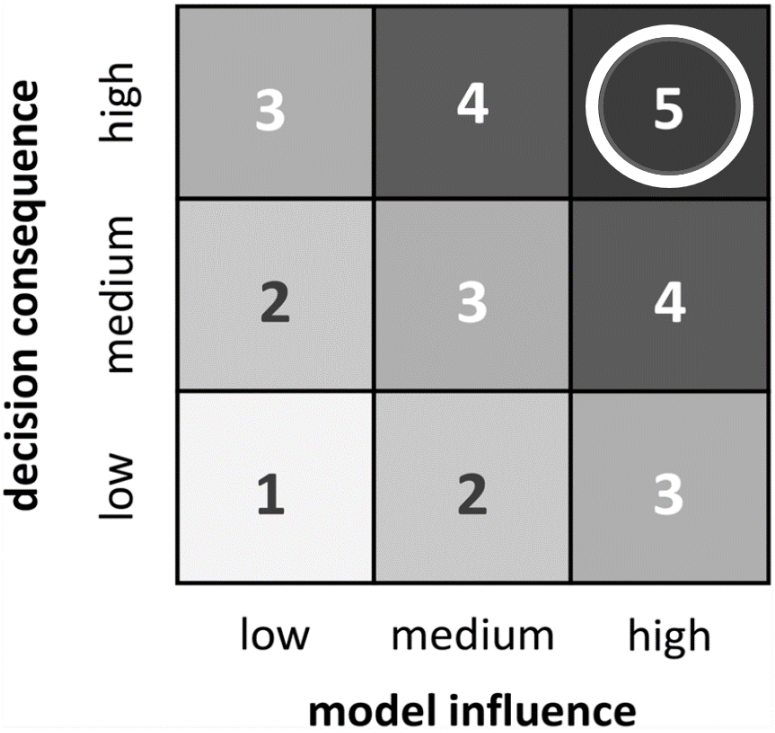

Fig. 1.11 Model risk assessment matrix: model risk for COU is HIGH - HIGH.

The comparator in this study was an experimental test in which tibial bearing was mounted into a potting material, and the talar component in a vertical moving arbor to

apply a five-times body weight load. Additional configurations were tested allowing the talar component to rotate.

The computational model reproduced the experiment substituting fixtures with boundary conditions. The tibial component was meshed with ten-nodes tetrahedron elements and the talar component with four-nodes quadrilateral elements. Nonlinear static analyses were performed using default convergence criteria and iteration methods.

1.5.1.1 **Credibility activities**

- Verification: Code verification was assured using a commercial code with many benchmark solutions. Calculation verification consisted in a mesh convergence analysis which assured that mesh size does not affect the quantity of interest results (contact area).
- Validation: model validation was performed comparing results from experimental test with the model predictions. A quantitative comparison showed accuracy to within 14% across all validation points.

In addition, sensitivity of the model was evaluated varying initial component positioning and material properties of polyethylene. The model has shown to be applicable to other similar geometries and flexion angles.

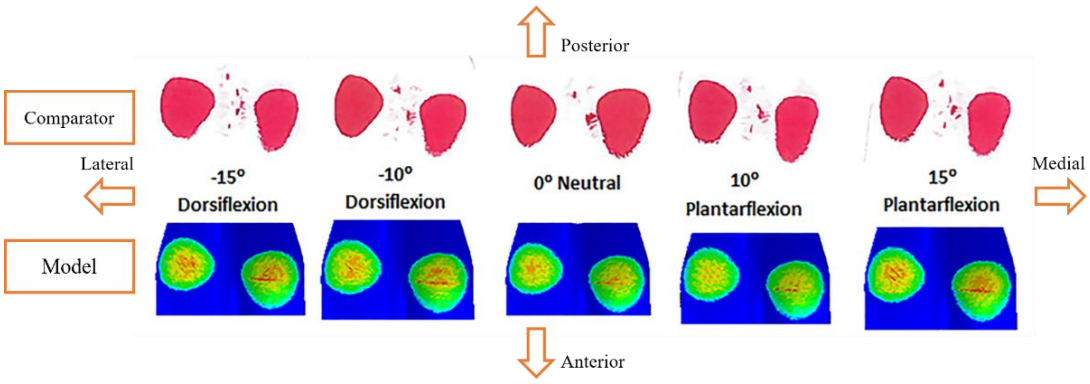

Fig. 1.12 Comparison in term of contact area

1.5.2 Mechanical properties of a femoral stem

In the study presented by (Wanki et al., 2020), a computational model was used as a design tool to assess if the desired porous stem stiffness was achieved. Fully dense stems frequently have mechanical issues like stress shielding. To overcome these complications, orthopedists are moving to compatible implants made of porous materials. Unfortunately, there is also the high probability of introducing uncertainties in the manufacturing of porous structures additive fabricated, resulting in significant uncertainties in the models used to predict the mechanical response of the porous implant.

- QOI: Has the desired porous stem stiffness been achieved?
- COU: The purpose of the computational model is to predict the mechanical response of the femoral stem (displacement and stiffness)

To assess the model risk associated with this COU, classification for model influence and decision consequence is proposed. Model influence and decision consequence are mapped to a five levels risk schema, as shown in figure (Fig. 1.11).

Model's influence is marked MEDIUM since the model's results will be used as a guideline for the prototyping phase that will be lately assessed through in vitro tests.

If the model leads to an incorrect design (under/overestimating the actual stem stiffness), surgery revision or patient injury could occur, which is associated to a HIGH level of risk. Based on this risk analysis, the COU has a model risk of MEDIUM-HIGH (level four in the model risk matrix).

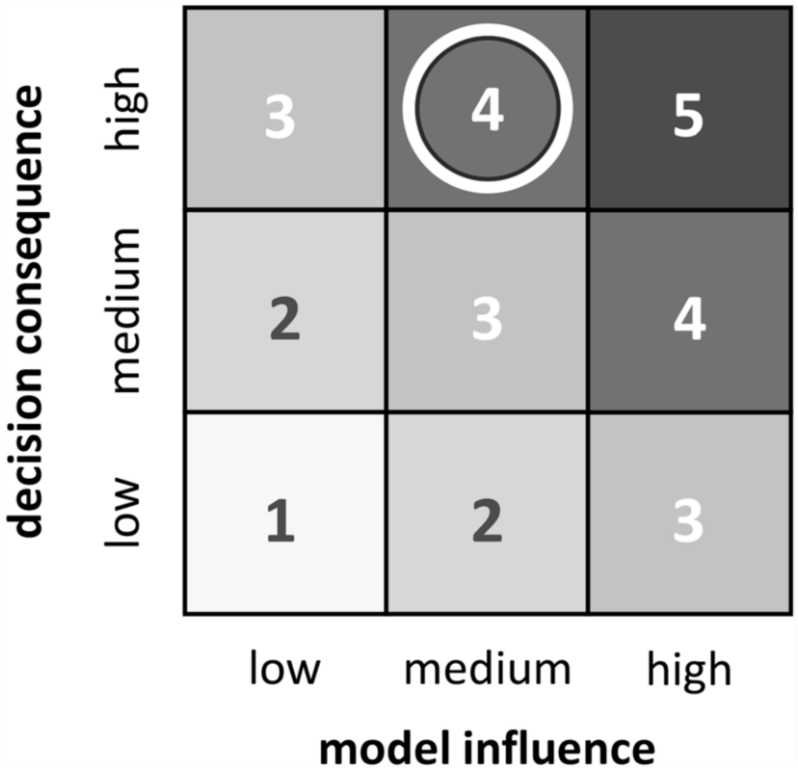

Fig. 1.13 Model risk assessment matrix: model risk for COU is MEDIUM-HIGH.

1.5.2.1 **Credibility activities**

The execution of the V&V plan was subdivided in five steps:

- Mesh sensitivity analysis of the FE model.
- Comparison of the FE model with numerical results for the same geometry.
- Statistical validation of the accuracy of the surrogate model.
- Comparison between the model prediction results and experimental data.
- Assessment of the relevance of the validation results to support the applicability of the model in the COU.

The first three steps of the V&V plan supported the verification process, the last two the validation and applicability processes.

- Verification: To perform code-to-code comparison the stem stiffness (quantity of interest) calculated with the proposed FE model was compared with the numerical solution available in (Jetté et al., 2018). For the surrogate model, the original FE model results and those for the quantity of interest were compared. To determine if the quantity of interest is sensitive to the mesh parameters, a grid convergence analysis was performed.
- Validation: The experimental tests were run following the ISO 7206-4 standard. Results for the porous stem stiffness calculated from the force and displacement diagram followed by their respective uncertainties were provided. The calculated relative difference between the experimental and numerical mean porous stiffness was around 11%. This agreement was considered satisfactory for this study.

The model has a probability to overestimate the real stiffness below 3%, whereas the probability to underestimate the actual stiffness is above 95%. However, preclinical (in vitro) tests are mandatory to confirm model predictions.

2 The BBCT pipeline

As mentioned in Section 1.2.1, areal Bone Mineral Density (aBMD) measured by Dual-energy X-ray Absorptiometry (DXA) is used as diagnostic criteria for osteoporosis. However, it is a moderate predictor of the femur fracture risk and does not capture the effect of some anatomical and physiological properties (e.g., three-dimensional geometry and distribution of the bone density) on the bone strength estimation. Most fragility fractures in fact occur in subjects with aBMD values outside the pathological range. The aim of BBCT pipeline is to increase predictive accuracy of osteoporosis detection, and to assist the process of evaluating the efficacy of new drugs. In this chapter, a detailed schematic description of the BBCT (Bologna Biomechanical Computed Tomography) is provided.

2.1 FE model

During this first step, the FE model is built starting from CT scan data of the whole femur (from the head to distal part until the tibial plate). The femur geometry is segmented and meshed considering subject specific material properties of the bone. Boundary conditions are then defined and applied to the FE model.

2.1.1 Geometry and Mesh

The geometry of bone is obtained dividing the femur from soft tissues and hip. To do so, commercial software ("3D Slicer image computing platform | 3D Slicer," n.d.; Mimics, n.d.) are adopted using a semi-automatic segmentation procedure. This procedure accounts for a sequence of common algorithms like thresholding, region growing and shrinking/growing. Once the three-dimensional geometry is obtained, the femur is meshed (Fig. 2.1) using a standard automatic meshing algorithm (ICEM CFD, Ansys Inc). The average element size is two millimetres, and the elements type is a ten-nodes tetrahedra named SOLID187 in ANSYS. This element type has a quadratic displacement behaviour and is well suited to model irregular geometries (e.g., femurs). Mid-side nodes for each element are included.

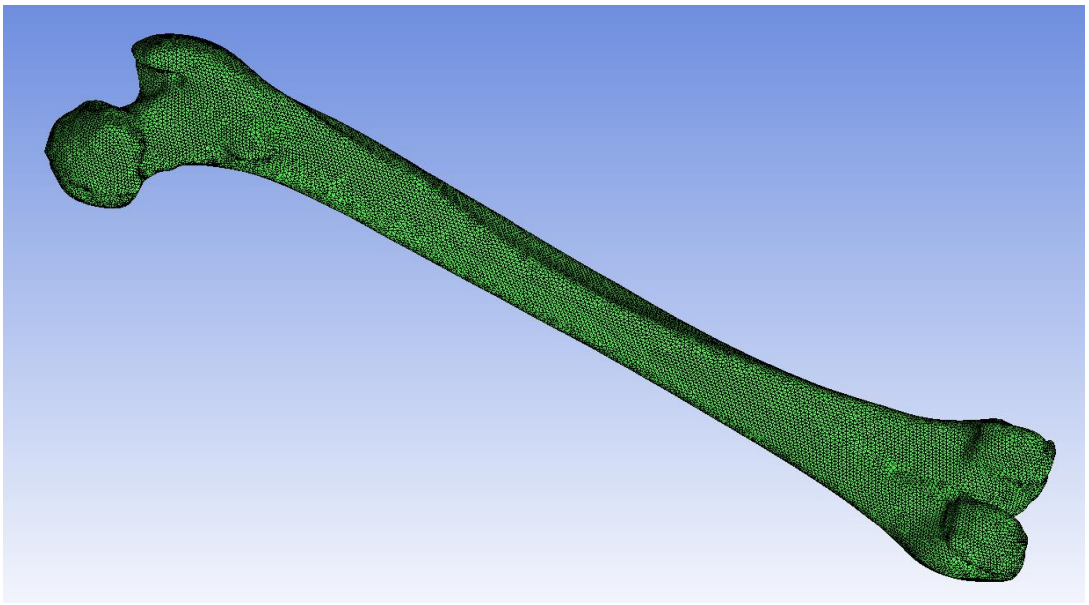

Fig. 2.1 Right femur meshed

2.1.2 Mapping material properties

Once the femur is meshed, material properties are assigned to each element. The material properties are, in brief, the elastic modulus E (MPa) and the Poisson ratio υ. Poisson ratio is fixed to 0.3 for both trabecular and cortical bone, and elastic module is calculated after a series of densities conversion.

Three different densities are taken into account:

- ρ_{QCT} (radiological density) which is calculated from the average Hounsfield Unit value (represents radiodensity, i.e. the inability of electromagnetic radiation to pass through a particular material) of all the voxels falling inside the specimen volume.
- ρ_{ash} (ash-density) which is calculated after the specimens were burned as ash weight/bulk volume.
- ρ_{app} (apparent density) which is density measured in fresh and wet conditions of the specimen.

The relationship between ρ_{QCT} and HU value is variable and depends on the CT scan parameters (e.g., kVp, exposure time, slice thickness and x-ray tube current). A linear regression can be obtained scanning an in-line phantom (QRM-ESP) with the same scan parameters used to acquire the CT data of the patient and by relating the calcium hydroxyapatite concentration of the five different phantom structures (three inserts that represent the spongious bone, the cortical structure and the spinal process) (fig. 2.2) to the corresponding mean value of the CT number extracted from the scan images of the phantom.

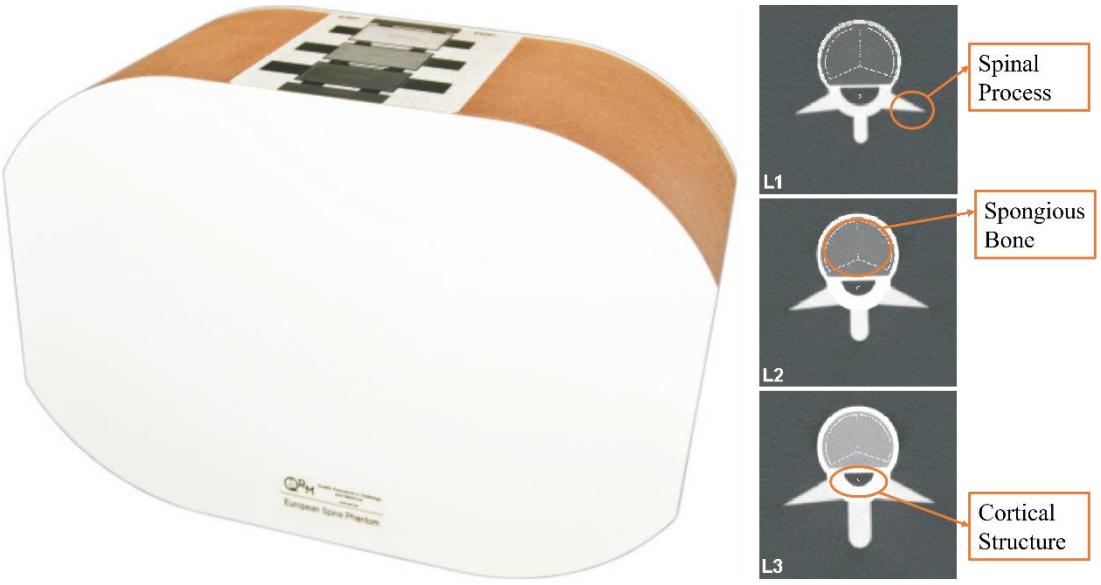

Fig. 2.2 Resin - based phantom body and QCT scans of the mid vertebral selections.

Based on the distribution of the CT values associated to each phantom structure, it is possible to obtain different calibration curves and define confidence intervals for the numerical coefficients (*a* and *b* in Eq. 2.1). In order to obtain ρ_{app} from ρ_{QCT}, two other relationships should be considered: from ρ_{QCT} to ρ_{ash} (Eq. 2.2) and from ρ_{ash} to ρ_{app} (Eq. 2.3). The elastic modulus (*E*) is then obtained (Eq. 2.4) with the widely used relationship (Morgan et al., 2003).

$$\rho_{QCT} = a + b\,HU \quad \text{(Eq. 2.1)}$$

$$\rho_{ash} = 0.877\rho_{QCT} + 0.079 \quad \text{(Eq. 2.2)}$$

$$\rho_{app} = \rho_{ash}/0.6 \quad \text{(Eq. 2.3)}$$

$$E = 6{,}850\rho_{app}^{1.49} \quad \text{(Eq. 2.4)}$$

Inhomogeneous material properties are automatically mapped (Fig. 2.3) onto the FE models using the BoneMat® software, which calculates an average Young modulus (E) for each element of the mesh, firstly converting each HU value into E and then performing a numerical integration over the element's volume.

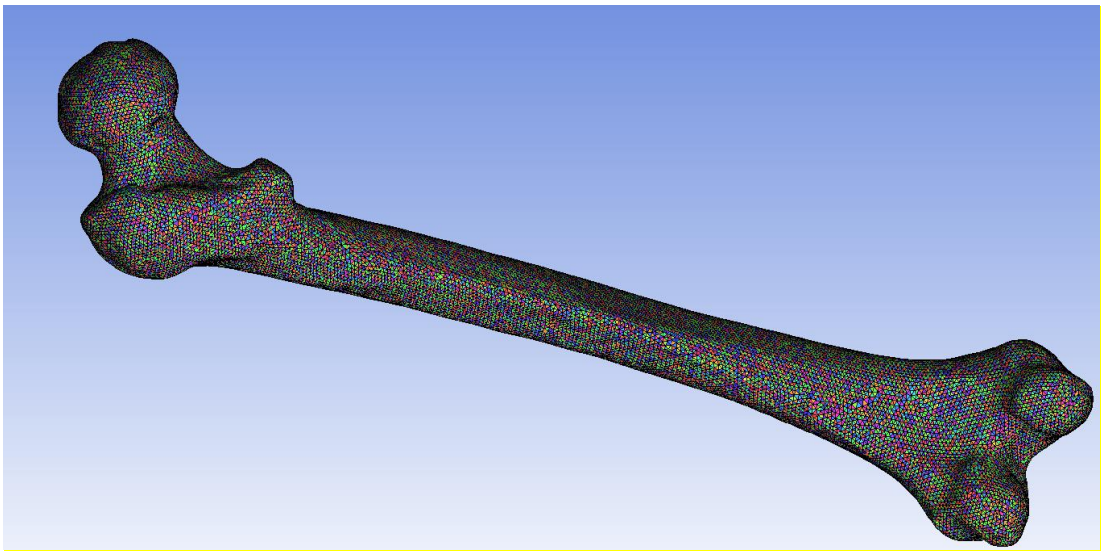

Fig. 2.3 Left femur with material properties assigned

2.1.3 Boundary conditions

In the sideways fall model, a totality of 28 different loading conditions were considered (tab. 2.1), varying force vector from -30° to 30° in two directions: posteroanterior and mediolateral.

label	Posantang (°)	Medlatang (°)
Neut	0	0
Ant10	10	0
Ant20	20	0
Ant30	30	0
Pos10	-10	0
Pos20	-20	0
Pos30	-30	0
Med10	0	-10
Med20	0	-20
Med30	0	-30
Ant10Med10	10	-10
Ant20Med10	20	-10
Ant30Med10	30	-10
Pos10Med10	-10	-10
Pos20Med10	-20	-10
Pos30Med10	-30	-10
Ant10Med20	10	-20
Ant20Med20	20	-20
Ant30Med20	30	-20

Pos10Med20	-10	-20
Pos20Med20	-20	-20
Pos30Med20	-30	-20
Ant10Med30	10	-30
Ant20Med30	20	-30
Ant30Med30	30	-30
Pos10Med30	-10	-30
Pos20Med30	-20	-30
Pos30Med30	-30	-30

Tab. 2.1 Loading conditions

These loading conditions should reproduce the most frequent loading scenarios due to a sideway fall (fig. 2.4).

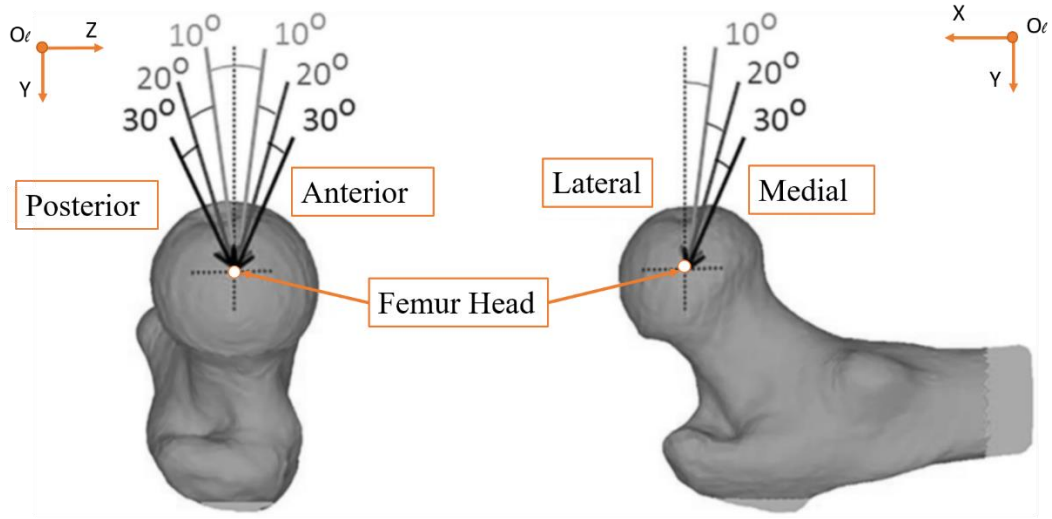

Fig. 2.4 Angles that define every possible force direction

Since a linear relationship is assumed between applied load and peak strain, the force entity is kept fixed to 1000 N (and later scaled) for all the sideways fall configurations and applied to the center of the femoral head. To find this latter and other useful anatomical landmarks, a virtual palpation analysis is conducted (fig 2.5).

To find the femur head center, a sphere is first fitted from a six-point cloud using an *ad hoc* Matlab script. The six points are the inferior and superior extremes of the box containing the femur head and identified in the three plane directions. Moreover, spatial coordinates of 4 anatomical landmarks on both medial and lateral condyle and epicondyle are captured. To do so, the femur geometry and the CT scan are loaded in 3D Slicer and the coordinate are captured positioning the cursor over the specific femur area. Processing those coordinates, an additional landmark in the knee center (Eq. 2.5) and directions (Eq. 2.6) for a local coordinate system (Eq. 2.7) are obtained (fig 2.5).

$$KneeCentre = \frac{LatCCond + MedCCond}{2} \quad \text{Eq. 2.5}$$

$$\begin{cases} XdirVec = \frac{FemurHead - KneeCentre}{15} \\ YdirVec = LatRCond - MedRCond \end{cases} \quad \text{Eq. 2.6}$$

$$\begin{cases} HeadDir = FemurHead + XdirVec \\ GrTrDir = FemurHead + YdirVec \end{cases} \quad \text{Eq. 2.7}$$

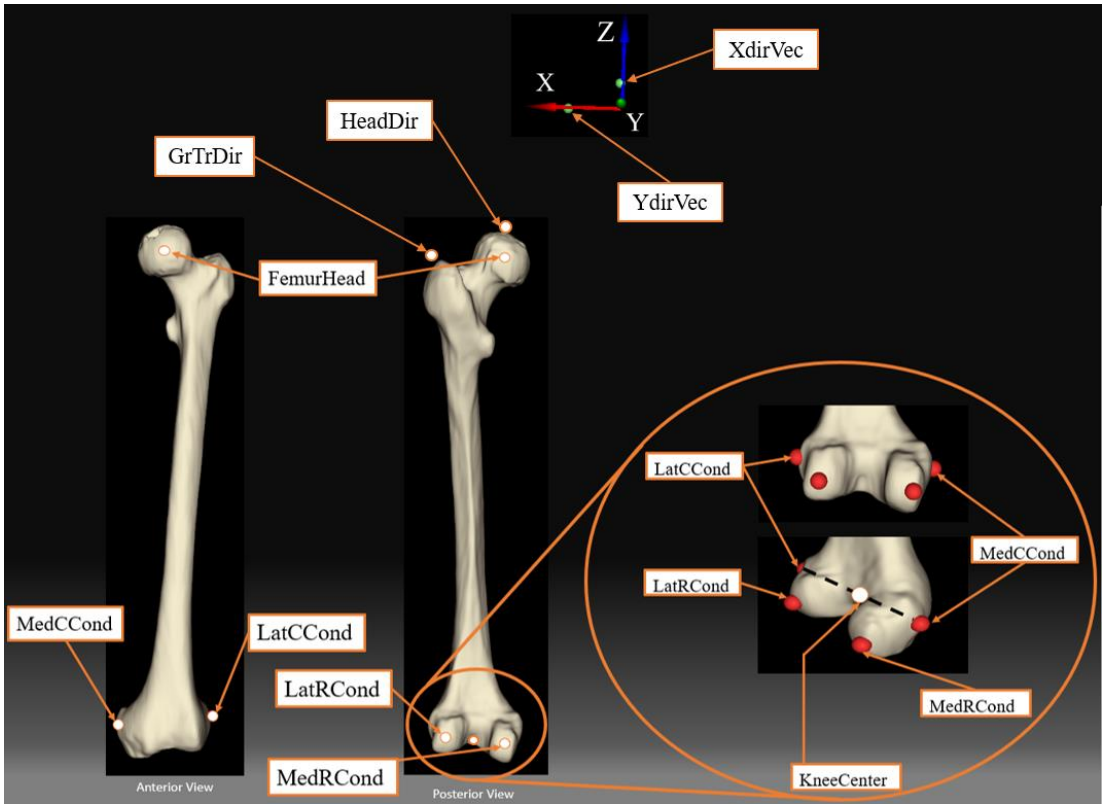

Fig. 2.5 Anatomical landmarks and reference system from virtual palpation

To represent the sideways fall configuration, the femur is constrained proximally and distally (fig. 2.6). Proximal and distal ends are divided during the simulation process by a cut plane perpendicular to the global z-axis, and whose location along femur shaft is identified through eq. 2.8. Distally, in the knee joint, only the rotational DoF around local z-axis is allowed. A multi-point constraint (mpc) approach is used to connect the distal end of the proximal femur with the center of the knee joint. The mpc region is a 4 mm string of nodes, two above and two below the cut plane passing through the point with z coordinate defined in Eq. 2.8 and orthogonal to the global z-axis. Proximally, the surface area of the greater trochanter slides without friction over an infinitely rigid plane, perpendicular to the local y-axis and passing through the most external node of the trochanter (along local y-axis direction). These boundary conditions make the structure isostatic.

$$cutPlaneZ = KneeCenterZ + (FemurHeadZ - KneeCenterZ) * 0.25 \quad \text{Eq. 2.8}$$

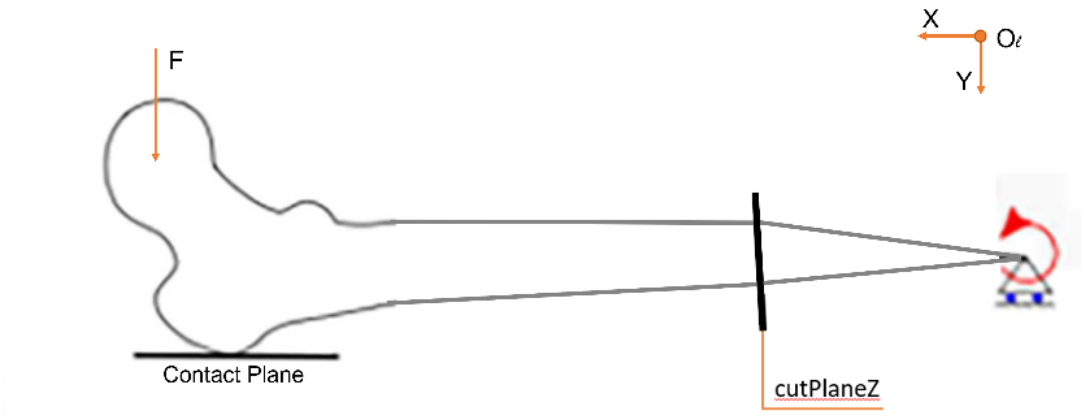

Fig. 2.6 Sideways fall configuration

2.2 FE simulations and result elaboration

Knowing the anatomical landmarks and the mechanical properties of the femur, sideway fall simulations are performed using ANSYS Mechanical APDL (Ansys Inc., PA, USA). First, a local reference system in the femur head is applied. To do so, the vectors XdirVec and YdirVec (eq. 2.6) are applied in the femur head. The local z-axis is the one that makes the system right-handed.

As said in Section 2.1.3, the rigid plane simulating the ground is constrained with a frictionless contact with the greater trochanter. Studying the contact between two bodies, the surface of one body is conventionally taken as a contact surface (the great trochanter) and the surface of the other body as a target surface (the rigid plane). In particular:

- All the elements of the rigid plane are type TARGE170 and define the target surface.
- All the elements comprised in a string of 4mm along local y-axis starting from the most external node (along the same axis) are type CONTA174 and form the contact surface.

The load is applied in the femur head center, and the direction for the Neut configuration is defined considering the axis passing through the greater trochanter and the femoral head center (fig 2.7).

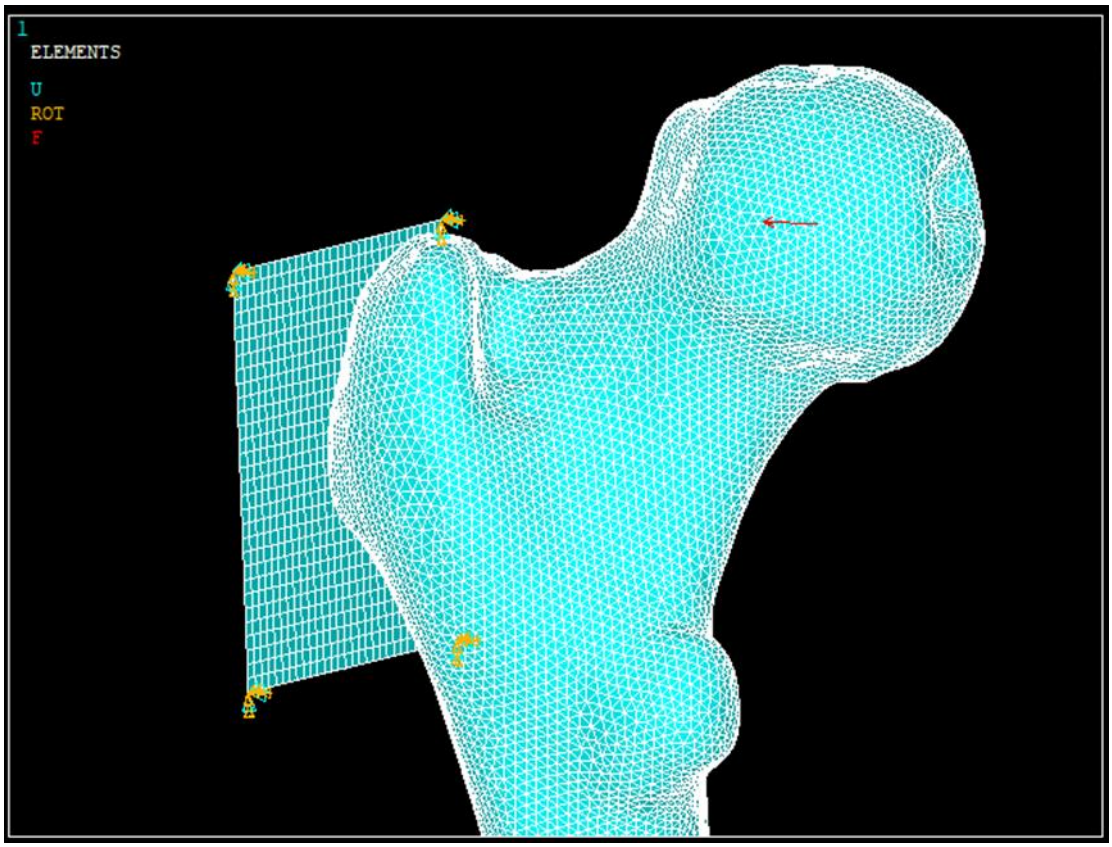

Fig. 2.7 Loading scenario

The contact algorithm used for the simulation is the augmented-Lagrangian, with those main features:

- Tolerance penetration factor of 0.1
- Symmetric contact behavior
- Damping allowed as a contact stabilizer
- Contact stiffness updating at every iteration.

The chosen equation solver is PCG (Preconditioned Conjugate Gradient), which is iterative like the sparse solvers but faster.

In the post-processing phase, principal total strain simulation results in both tension and compression are stored for each node, and their location as well. In order to avoid boundary effects, only nodes in a region of interest (ROI) are considered (grey region in fig. 2.8). The ROI for this simulation consist in the nodes of the femur external surface without:

- All elements that are below a plane perpendicular to the global z-axis and located under femurHeadZ of a quantity equal to a quarter of the distance between femurHead and kneeCenter, along global z-axis.
- The contact surface (orange region in fig. 2.8).

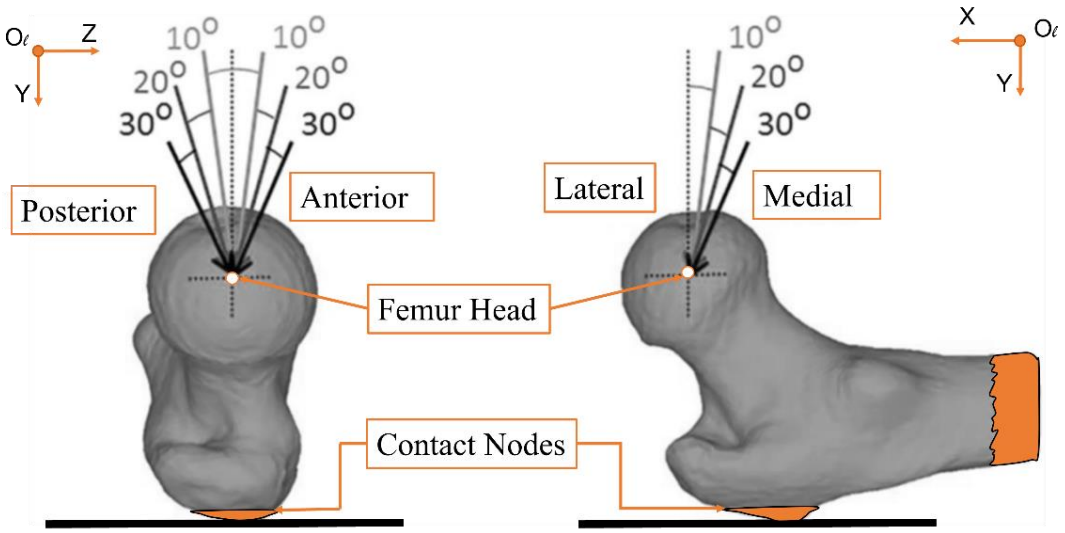

Fig. 2.8 ROI considered for the result elaboration

To estimate femur strength, a maximum principal strain criterion is adopted. According to this latter, principal strains are:

- averaged at the surface nodes on a circle of 3mm radius, thus avoiding unexpected local effects (better explained in Section 3.3.1)
- normalized with a factor of 0.73% and 1.04% for tensile and compressive strains respectively, to compare themselves.

Done that, a modified strain matrix is built, where among the normalized strains (tension and compression) only the higher value is considered for each node. Failure node is thus identified as the one with the highest strain value associated, as well as the modality of failure. Failure load of the femur is calculated as the ratio of the applied load (1000 N) and the failure strain. Minimum fall strength (MSF) is the minimum value across all the failure loads obtained considering all the simulated loading directions (Tab. 2.1).

As reported by (Bhattacharya et al., 2019), the absolute risk of fracture at time zero (ARF0) is defined as the probability that the patient will fracture over the same period, and thus that at least one of the several fall conditions will result in a fracture. To calculate the probability of fracture, failure (critical) load values are plotted as a function of both posteroanterior and mediolateral angle (fig. 2.9).

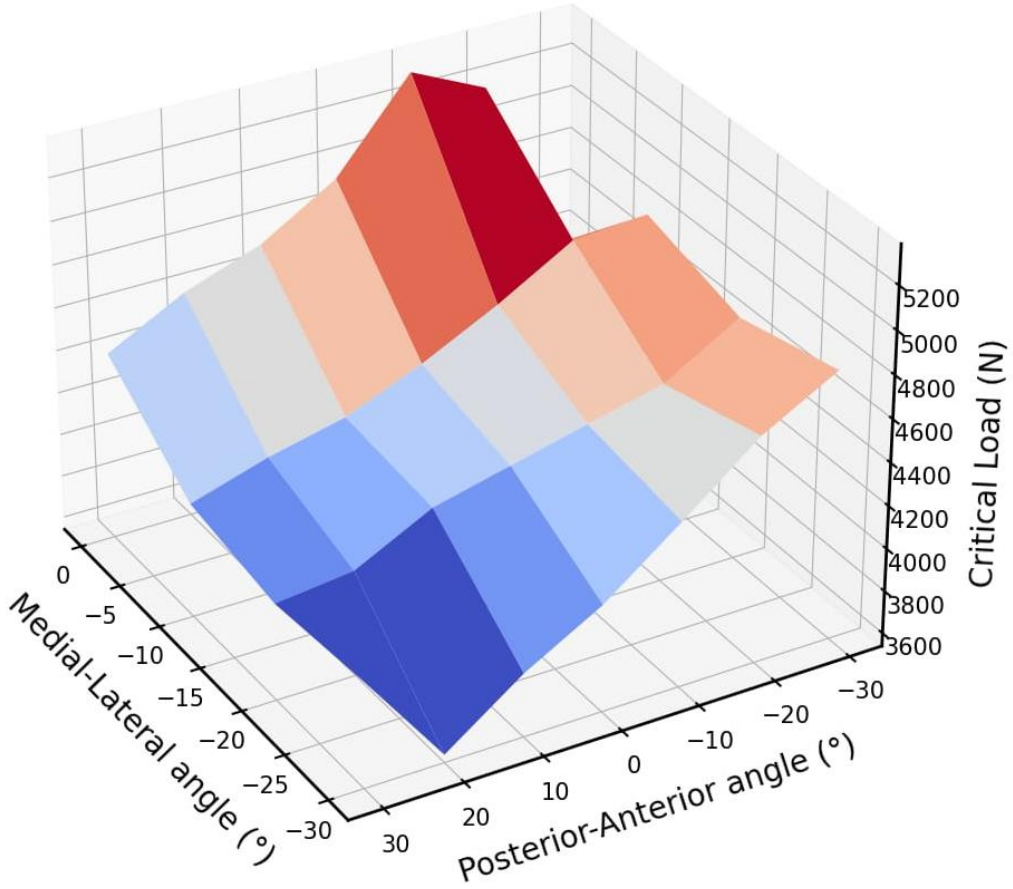

Fig. 2.9 Failure load as a function of mediolateral and posteroanterior angle

A million of possible patient specific impact loads during a fall (fig 2.10) are generated considering patient height and weight and using an inverse latin hypercube stochastic sampling over six gaussian input variables.
The multiscale model accounts for whole-body dynamics during a fall and hip impact with the ground. The body-floor impact model is able to assess the magnitude of impact force during a fall, idealized as a rotation of the whole body on any plane containing the vertical axis, like a mass (m) concentrated at the moving end of an inverted pendulum. The rotation occurs around a spherical joint (hinge) fixed to the floor and located near the foot on the side of impact. The velocity of impact (u) is obtained calculating the total kinetic energy per unit body mass (e) at the end of the fall, reduced by the work done by the lower limb muscles that activate during fall. The peak of impact force is finally calculated as (eq. 2.9):

$$F^* = mu/\Delta t \qquad \text{Eq. 2.9}$$

Where Δt is the total impact duration. The attenuated peak impact force magnitude applied to the greater trochanter (eq. 2.10) is evaluated accounting for two factors:

- η_I damping due to flooring elements and all active soft tissues (muscles)
- η_{ST} damping due to all passive soft tissues interposed between the point of impact on the skin and the lateral aspect of the greater trochanter.

$$F = (1 - \mu_{ST})(1 - \mu_I)mu/\Delta t \qquad \text{Eq. 2.10}$$

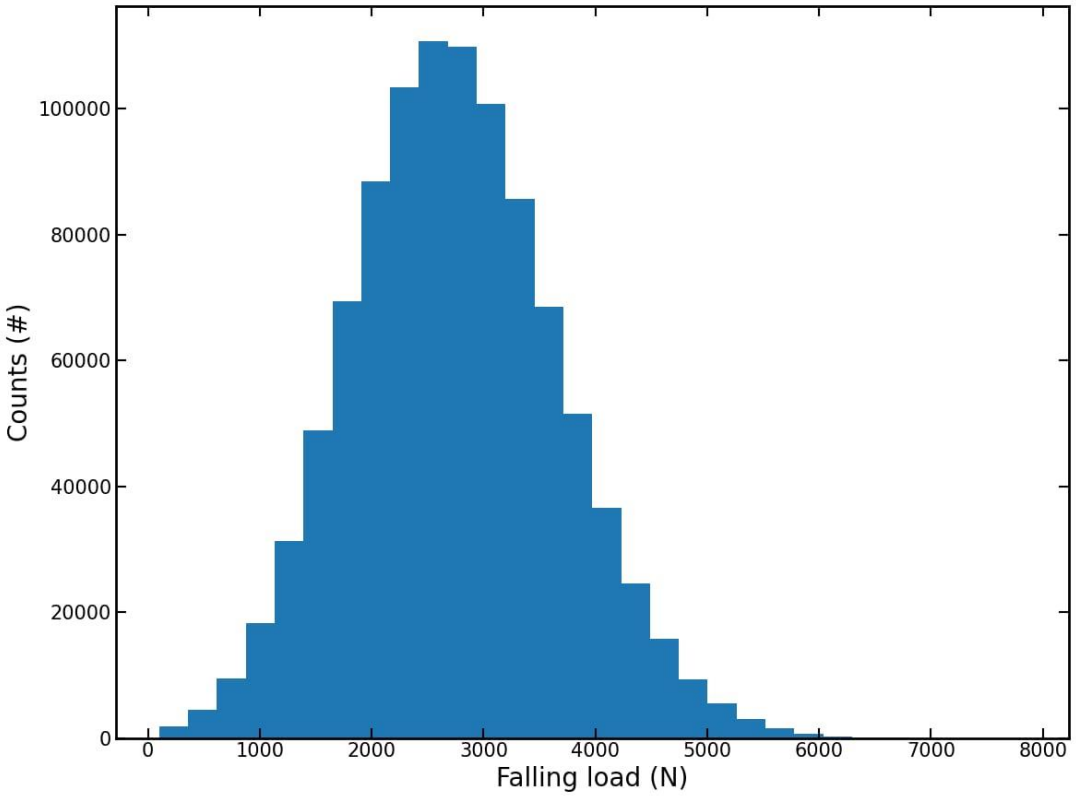

Fig. 2.10 Distribution probability of loads over one million falls

Comparing the critical load with a million of possible loads during a fall, fracture probability for each of the 28 angles is obtained (fig 2.11).

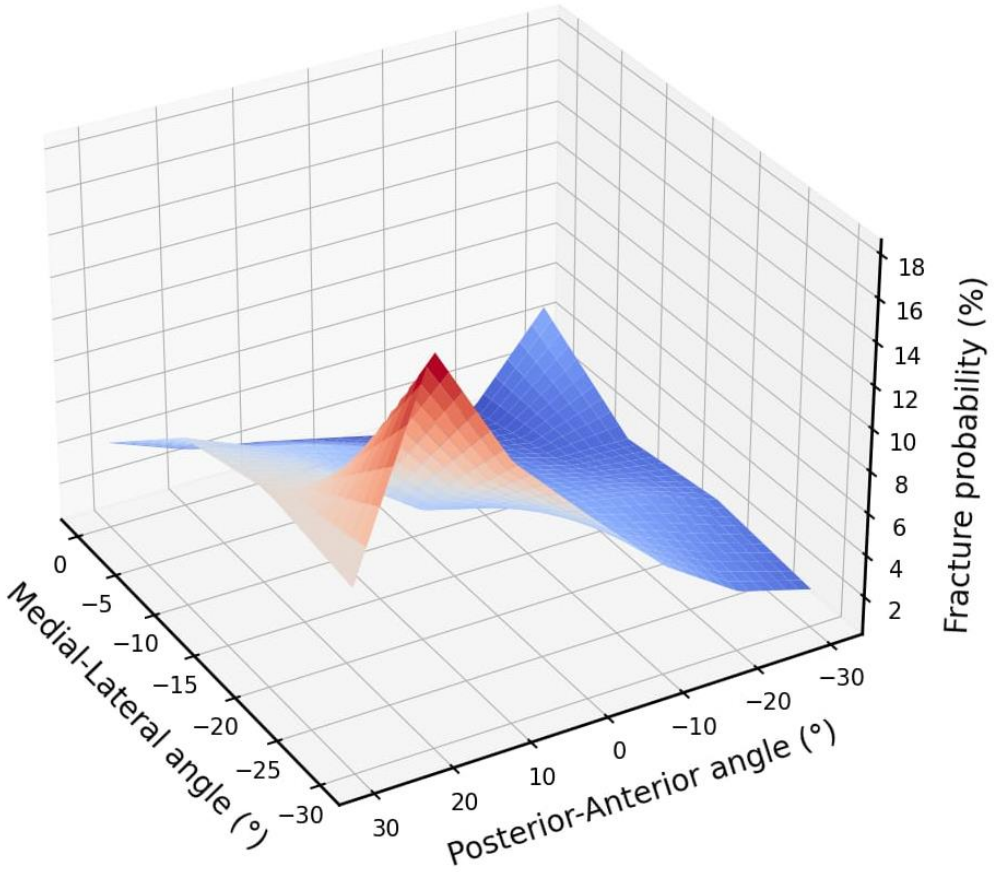

Fig. 2.11 Fracture probability as a function of mediolateral and posteroanterior angle

Fracture probability curve is then bilinearly interpolated (to obtain its surface) and integrated to calculate the average fracture probability after a fall (*fracProb*). Eventually, using eq. 2.11, ARF0 can be calculated.

$$ARF0 = (1 - (1 - fracProb)^{riskExp}) * 100 \qquad \text{Eq. 2.11}$$

The value *riskExp* (risk exposure) is the estimated value of fall probability over the period of one year, and it is equal to 0.65.

3 Verification and Validation activities plan

In the following chapter, a detailed explanation of the performed credibility activities is provided. When necessary for sake of clarity, more than one femur from different patients was modelled, but in general all credibility analyses were conducted on the same femur. As the ASME V&V-40 2018 guidelines suggest, the credibility assessment is risk informed and thus the question of interest (QOI), context of use and model risk are first defined.

- QOI: Is the new antiresorptive drug effective to reduce the femur fracture risk?
- COU: BBCT-derived ARF0 is used as a surrogate biomarker of the primary endpoint proximal femoral fracture in phase II and phase III clinical trials to evaluate the efficacy of a new antiresorptive drug, in place of the measured DXA-based aBMD.

To assess the model risk associated with this COU, a classification for both model influence and decision consequence is proposed (fig 3.1).

Model influence is HIGH, since the output from the computational model (ARF0) is a significant factor, prevalent on other evidence (e.g., bone density measurements), to inform the decision.

Decision consequence is MEDIUM because an incorrect decision could result in a moderate impact for the patient (e.g., a new drug successfully pass through several stages of clinical trials and is approved by the regulatory authority for use but it is not effective).

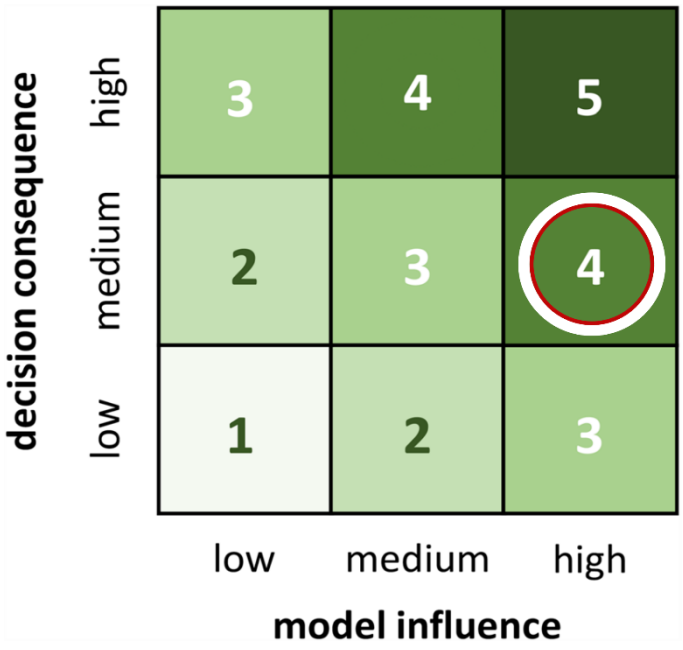

Fig. 3.1 Model risk assessment matrix: model risk for COU is HIGH - MEDIUM.

3.1 Case studies

For the following analyses four patients from HipOp archive were enrolled. HipOp is an archive where, from year 2014 to 2019, 5000 CT scans were collected, together with general information such as age (at the time of the exam), gender and body measures (height and weight). Data are collected to evaluate the course of disease, and to assess necessity of surgeries like total hip arthroplasty. Since a DXA scan was not available for the cohort, a QCT-based projection was used to estimate aBMD.

3.1.1 Cohort selection

For the following analyses three anonymized patients were enrolled, and their generalities are summed up in tab. 3.1.

Patient Code	Gender	Dead/ Alive	Age (yrs)	Height (cm)	Weight (kg)	Femur	aBMD $\left(\frac{g}{cm^3}\right)$	T-score
D0062	Woman	Dead	66	163	56	Left	0.916	-0.213
L121	Woman	Alive	64	140	45	Left	0.726	-1.77
L122	Woman	Alive	81	156	53	Left	0.769	-1.418
L123	Woman	Alive	77	168	59	Left	0.675	-2.188

Tab. 3.1 Characteristics of the patients considered for the study

3.1.2 CT scanning procedures

The patients enrolled in HipOp register were scanned with several different multidetector CT, and each scan was performed with different parameters. To take account of these variabilities, a totality of twenty different regression lines is available, evaluated scanning the QRM-ESP with different combination of the main parameters (kVp, exposure time, slice thickness and x-ray tube current). In the following table (tab. 3.2), those parameters for the study cohort are summed up.

Patient Code	Slice thickness (mm)	Peak Kilovoltage (V)	Exposure time (s)	x-ray tube current (mA)
D0062	3	120	1000	200
L121	2.5	120	1724	150
L122	2.5	120	1724	150
L123	2.5	120	1724	150

Tab. 3.2 Overview of cohort scanning parameters

3.1.3 Exclusion criteria

From CT scan was possible to assess if the scan showed metal artifacts, or if the patient suffered of osteoarthritis in one or both femurs. When the arthritis was evident, the patient was operated in a total hip arthroplasty. The femur was not segmented if one of those two conditions was present.

3.2 Force and moment equilibrium

To do this verification activity, two analyses were conducted. The constraints of the femur are one hinge in the knee joint center and a surface – surface contact between the great trochanter and the ground. Since the contact between femur and plane constraints one translational DoF, the contact is replaced with a carriage constraint positioned on the most external node of the trochanter. Even if this is a three-dimensional problem, in the local reference system one direction of the forces is prevalent on the other two thus allowing to be schematized for guidance only as in fig. 3.2. The femur has in total 6 DoF, the hinge removes five of them and the carriage the last one (vertical). Therefore, this is an isostatic problem. Force equivalence can be conducted both in local and in global coordinate system, in the following analysis for the sake of simplicity counts are considered in local system.

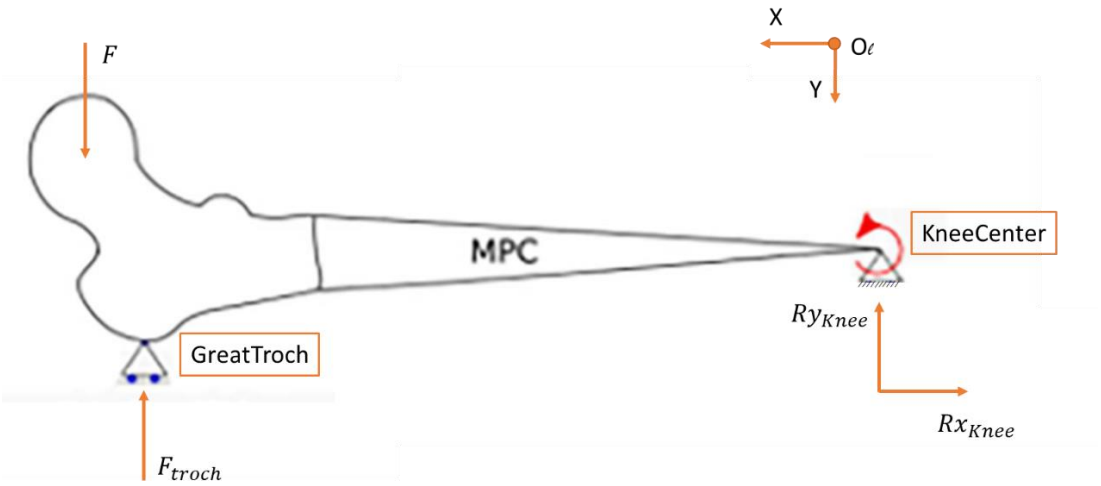

Fig. 3.2 2D Schematization of the force equilibrium problem.

3.2.1 Force equilibrium

This check assures that the applied force is equals to the reaction force. The reaction forces were extracted for both the constrained nodes (F_{troch} and R_{knee} at the greater trochanter and knee joint center respectively) and summed to the load applied at the femur head (F).

Firstly, the coordinates of femur head center, greater trochanter node and knee center node were extracted from the model. Then, in accordance with the directions of the forces, vectors were summed together as in eq. 3.1.

$$F_{tot} = -F + F_{troch} + R_{knee} \qquad \text{Eq. 3.1}$$

3.2.2 Moment equilibrium

To calculate moment equilibrium, the lever arm of the three nodes with respect to the local coordinate system is extracted from the model, as well as the concentrated moment on the knee (M_{conc}). The moment exerted by each force (M_{Head}, M_{Knee} and M_{Troch} applied at the femur head, knee joint center and great trochanter respectively) is determined performing the cross product between the force and the lever arm. The resultant is calculated adding the moment exerted by forces with the concentrated one on the knee, as in eq. 3.2.

$$M_{tot} = -M_{Head} + M_{Knee} + M_{Troch} + M_{conc} \qquad \text{Eq. 3.2}$$

3.3 Mesh convergence study

As said in section 1.4.3.1, mesh convergence analysis assures that the quantities of interest (in our case principal total strain) extracted from the FE analysis are not affected by element edge size, and thus by the total number of DoF of the model. It is commonly accepted that if the QOI converges asymptotically to a value x by increasing the number of the model DoF, the solution from the finite element method converges to the exact solution of the underlying partial differential equation. Every FE simulation must have the same boundary conditions, and the QOIs evaluated in the same position in a homogenous structure. Mesh convergence analysis assessed in this way is said to be conducted "according to Patch Test" (Zienkiewicz et al., 2005).

In our case, a typical standard mesh convergence analysis based on patch test was not performed because of the heterogeneous nature of the models and the dependency between mesh size and mechanical properties of the material. However, a sensitivity analysis was conducted varying the mesh element size to find the right mesh density needed to reduce the discretization error.

Analyses were conducted for three different femur geometries from three different patients following the procedure below:

- After result elaboration, the modality of failure (tension or compression) was identified
- Based on the failure mode, for the most refined model the node with highest principal total strain (ε) was considered, and both strain value and node location were extracted.
- In the same location, the value of ε was extracted for all the other models with coarser mesh.

Since for all femurs of the cohort the modality of failure was compression, from now on ε can be used in place of third principal strain (fig. 3.3).

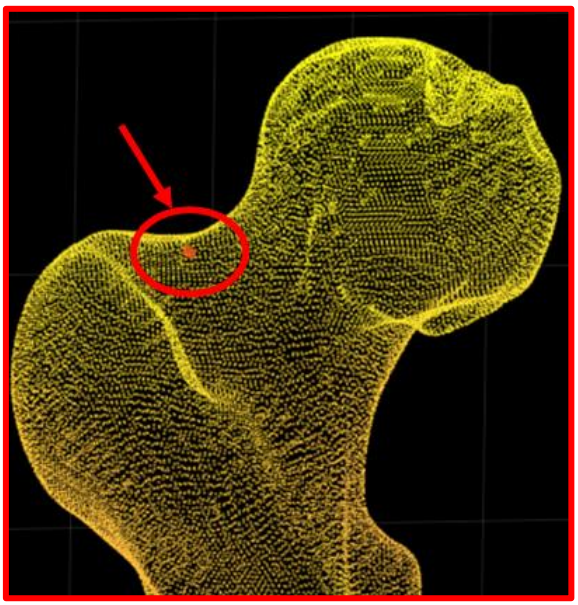

Fig. 3.3 Max strain node location was in the upper side of the neck for the three femurs.

Convergence was checked computing the percentage differences $d_\varepsilon(\%)$ according to the eq. 3.3:

$$d_\varepsilon{}^i = \left|\frac{\varepsilon^{i*}-\varepsilon^i}{\varepsilon^{i*}}\right| \cdot 100 \qquad \text{Eq. 3.3}$$

where superscript *i* refers to models with progressively smaller element edges listed in tab. 3.3. The results obtained with the most refined model ($i^* = 5$) were considered as reference solution. Femur L121 was excluded from this and latter analysis because, for the elements including the node in femur head, the Jacobian ratio (see section 3.6) became negative for the mesh with element size 0.75. This issue was responsible of the non-convergence of contact algorithm.

i	N_{DoF}			e_{size} (mm)
	D0062	L122	L123	
1	140865	132177	136047	4
2	324969	302715	312522	3
3	1065255	992823	1025067	2
4	8360421	7802310	8035176	1
5	19634724	18296130	18970344	0.75

Tab. 3.3 Example of a mesh refinement scheme used for the convergence check. Legend: i = model ID, N_{DoF} = number of degrees of freedom, e_{size} = maximum element size.

Convergence was assumed for percentage differences of the predicted strain value inferior than 10%.

Another important convergence study was conducted on the failure load (FL) quantity following the refinement scheme reported in Table 3.3 and computing the percentage difference ${d_{FL}}^{i}$ (%) with respect to most refined model. The main differences between this analysis and the other is that the quantity of interest is here post-processed, since the principal total strains were mediated into a circular volume of 3mm radius. As said before (see section 2.2) the failure node is the maximum normalized value of the modified strain matrix, therefore its location change depending on the element size because also material properties change. Since the failure load is evaluated in the failure node, also its point of application can change, even if few millimetres.

Convergence was checked computing the percentage differences $d_{FL}(\%)$ according to the eq. 3.4:

$$ {d_{FL}}^{i} = \left|\frac{FL^{i*} - FL^{i}}{FL^{i*}}\right| \cdot 100 \qquad \text{Eq. 3.4} $$

3.3.1 The D0062 case study

For one femur of the cohort, further analyses were conducted in order to find an explanation to its non-convergent behaviour on the third principal strain quantity. Results of these analyses will be presented in the next chapter.

For each one of the five different edge-length femur mesh, a cluster of elements attached to the node with maximum strain was considered. For those elements, two quantities of interest were extracted:

- Strain energy density (J/m^3)
- Elastic moduli (MPa)

Strain energy density (SED) is a non-negative scalar value that provides the relationship between energy employed to deform a volume and imposed strain. SED was extracted for all elements in the maximum strain node.

Among the same cluster, average value and standard deviation of these quantities were calculated, and later compared between the clusters.

Since the results of these analyses showed an anomalous behaviour for elastic moduli, a border effect was suspected (fig. 3.4). A border effect is a consequence of a bad local segmentation, where the segmented femur geometry does not accurately follow the real one (from the CT scan). When this happens, one or more elements of the mesh do not belong to the femur, but to the soft tissues instead. Therefore, very low mechanical properties are assigned to those elements, biasing the results. To confirm this hypothesis, two further mesh convergence analysis were conducted for the same femur. In the first one, mesh convergence was evaluated in a different node close to the one with maximum strain. In the second, a new geometry from a different

segmentation was considered, paying attention to accurately reproduce the real cortical surface in the region of interest.

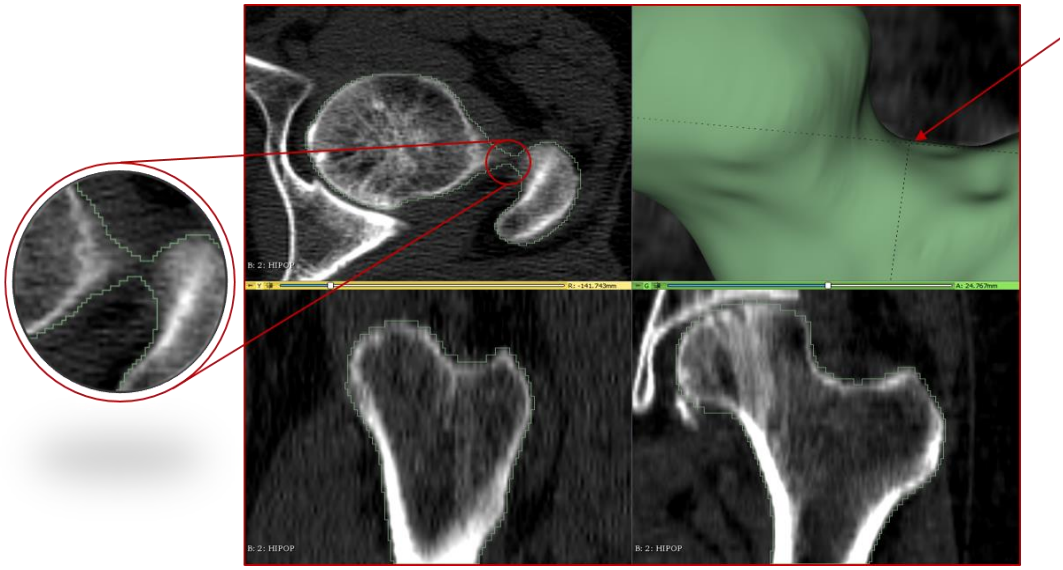

Fig. 3.4 Suspected location for border effect

3.4 Effect of uncertainties in material properties mapping

These analyses aim to assess the effects on the quantity of interest of uncertainties linked to material properties assignment. To do so, several phases of the mapping step were identified, and an analysis was conducted for each of them:

- Uncertainties in HU distribution
- Uncertainties in phantom segmentation
- Uncertainties in phantom choice
- Uncertainties in Morgan relation

Some of these analyses were conducted following the main principle of the Taguchi method (a widely used statistical model) of Design of Experiment (DOE). According to this method, it is possible to investigate problems with a large number of parameters and obtain important information about system behaviour with a limited number of experimental tests (Montgomery, 2017). In particular, the multi-variables system behavior can predicted investigating vertices.

3.4.1 Uncertainties in HU distribution

This analysis was conducted to evaluate the effect of the distribution of Hounsfield unit (HU) in the CT scan of the calibration phantom on the simulation results. In other words, to what extent slope and intercept of the linear regression line can be affected.

To do so, two different segmented geometries of the same QRM-ESP phantoms were considered. The first one followed the real contours of the CT images, and the second one was derived by the first performing a shrink of 4.4 mm (fig. 3.5). Each geometry consists in five different segments, three vertebrae, one cortical structure and one spinal process. All those segments had different values and distributions of HU among the same segments.

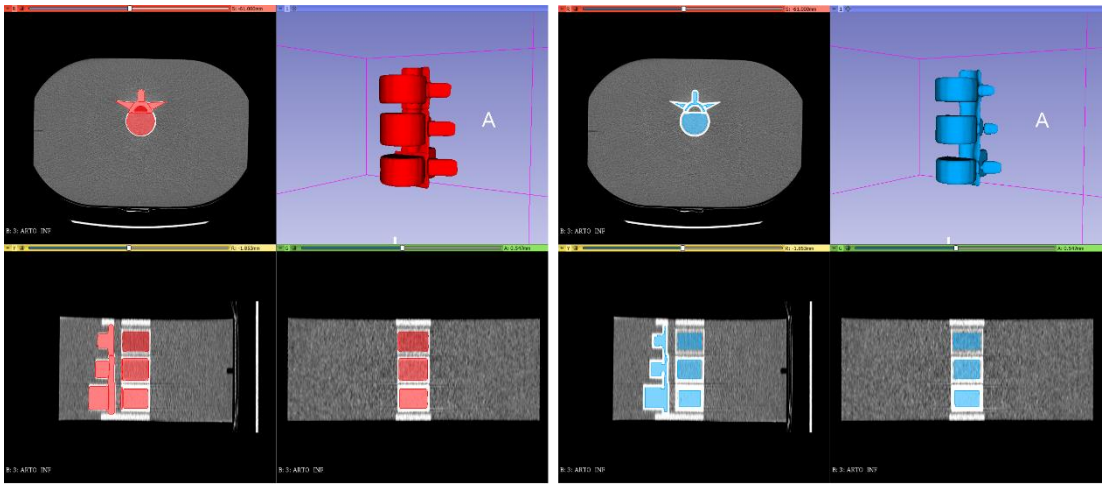

Fig. 3.5 Calibration Phantom (red volume) and after shrink (blue volume)

Once those two segmentations were obtained, a binary labelmap was extracted as well as the regression lines using a custom matlab script (fig. 3.6 and fig. 3.7).

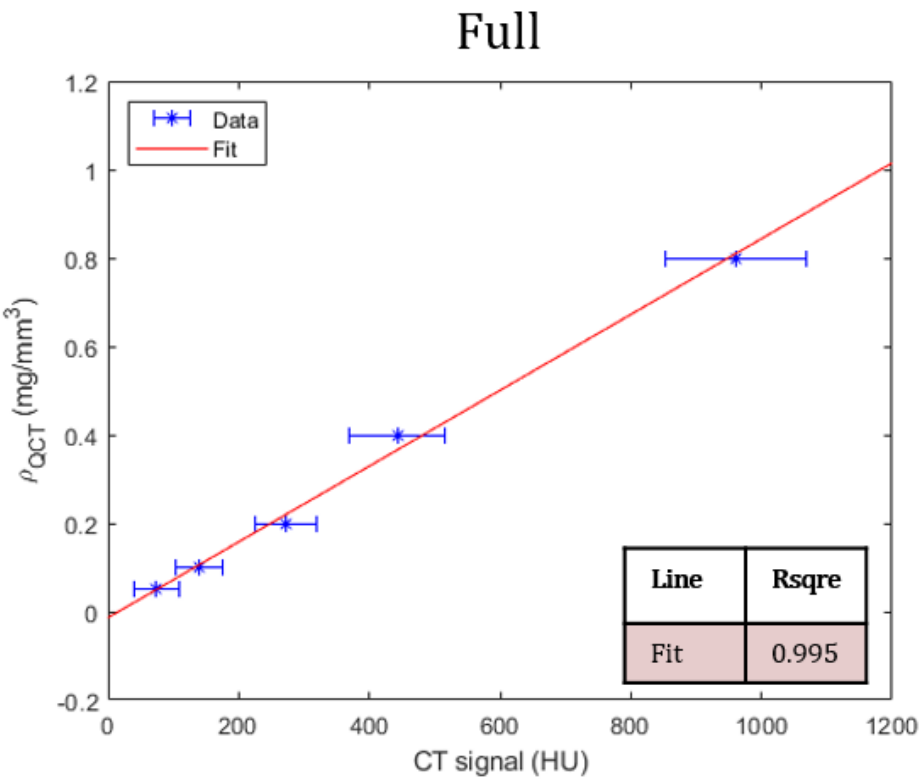

Fig. 3.6 Regression line of full phantom

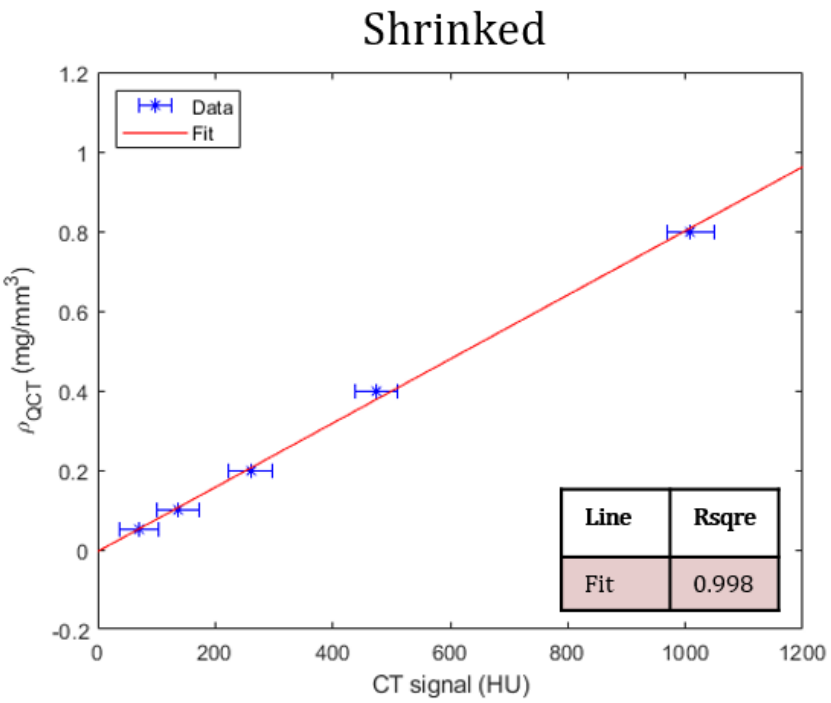

Fig. 3.7 Regression line of shrinked phantom

As the picture above shows, the regression lines were extracted using the mean value of the HU distribution intervals, one for each segment of the phantom. As expected, error bars for the shrinked phantom was smaller than the full one. For each phantom, two additional regression line were extracted using the two endpoints of the distribution intervals (fig 3.8 and fig. 3.9). The three lines (max, med and min) defined an area on the graph.

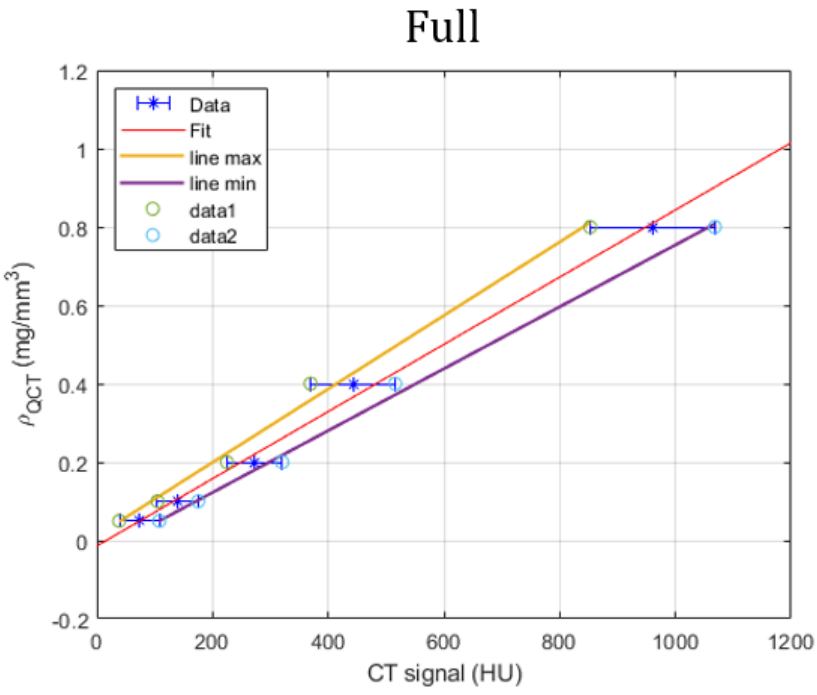

Fig. 3.8 Area of uncertainty defined by the three regression lines (full phantom)

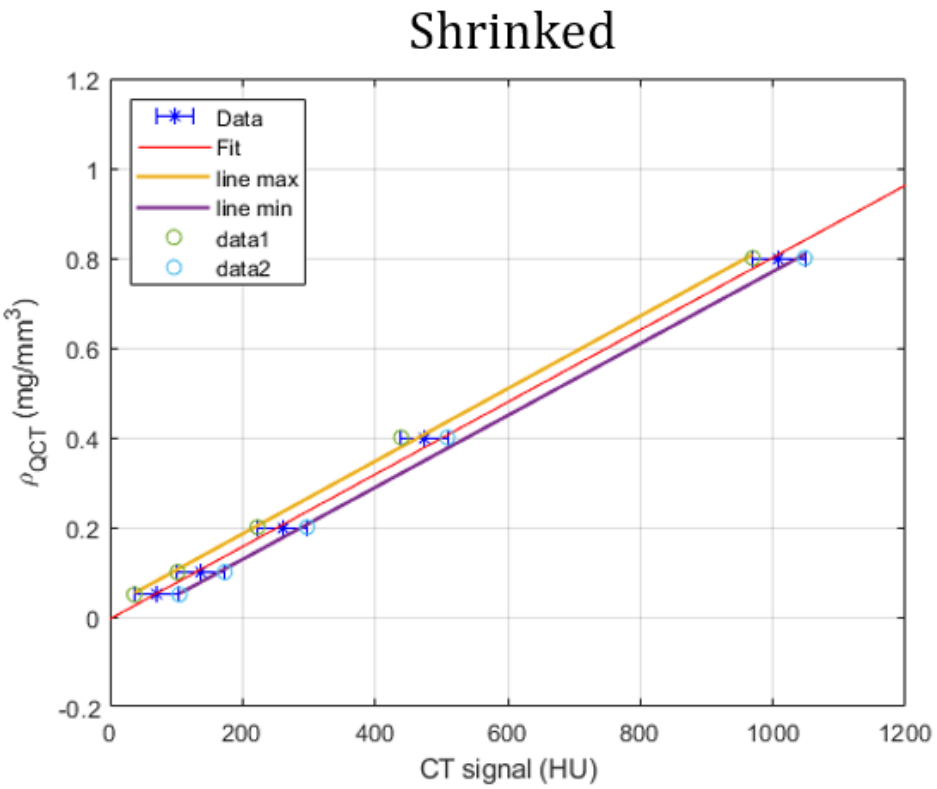

Fig. 3.9 Area of uncertainty defined by the three regression lines (shrinked phantom)

To assess uncertainty in HU distribution, six different models using the six different regression lines were built, and the percentage error, evaluated in terms of principal total strain, was calculated for the same node with eq. 3.5.

$$e_\varepsilon{}^i = \left|\frac{\varepsilon^{i*}-\varepsilon^i}{\varepsilon^{i*}}\right| \cdot 100 \qquad \text{Eq. 3.5}$$

Superscript *I* refers to models with modified calibration line (max or min). The results obtained with the median calibration line (i*) were considered as reference solution.

3.4.2 Uncertainties in phantom segmentation

This analysis was conducted to evaluate the inter-operator uncertainties in the regression line that arise when the same phantom is segmented by different users. As said in section 3.1, twenty different calibration lines are available and each one refers to different scan parameters. From past analyses, data regarding calibration phantom n°1 were available. This phantom was segmented by five different operators, obtaining five different couples of slope (b) and intercept (a). A variation coefficient as in eq. 3.6 was calculated and used to reproduce the uncertainty range for phantom n°12, which was the one used for our simulations (fig. 3.10 and 3.11).

$$CV = \left|\frac{St.Dev}{Mean}\right| \cdot 100 \qquad \text{Eq. 3.6}$$

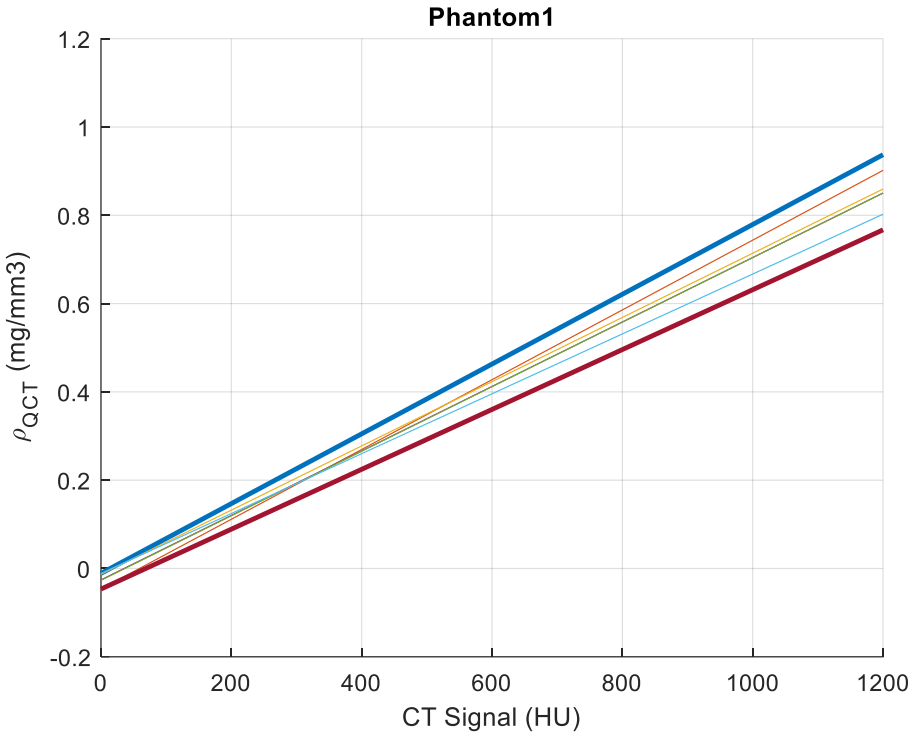

Fig. 3.10 The five different calibration lines for phantom 1

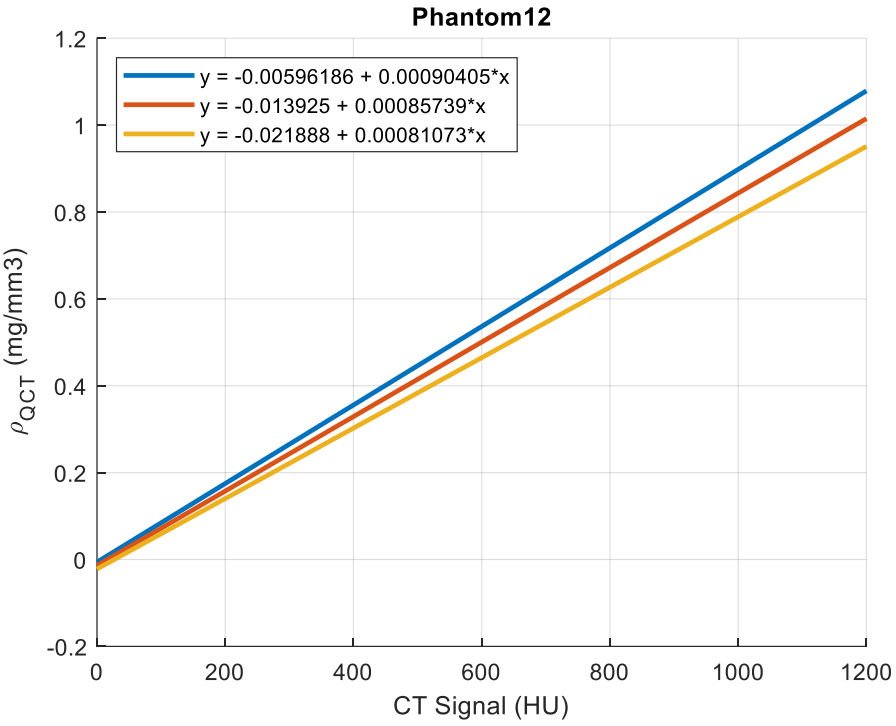

Fig. 3.11 The area of uncertainty in phantom 12

From each calibration line (fig 3.11) three models were built and the percentage difference, evaluated in terms of principal total strain, was calculated for the same node with eq. 3.7.

$$d_{\varepsilon}{}^{i} = \left|\frac{\varepsilon^{i*} - \varepsilon^{i}}{\varepsilon^{i*}}\right| \cdot 100 \qquad \text{Eq. 3.7}$$

Superscript *I* refers to models with modified calibration line (max or min). The results obtained with the median calibration line (i*) were considered as reference solution.

3.4.3 Uncertainties in phantom choice

This analysis was conducted to assess the uncertainties that can arise choosing the calibration phantom. Indeed, during the material properties mapping, one among the twenty calibration lines is selected basing on similarity of the main scan parameters. To each parameter, a weight basing on its importance to inform the decision was assigned (tab. 3.4). A comparison value (that runs between one and ten) named calibration score was calculated basing on those weights, and the calibration phantom was chosen basing on it.

Parameter	**Weights**
Slice thickness	1
Peak Kilovoltage	6
Exposure time	1
x-ray tube current	2

Tab. 3.4 Weight of each scan parameter to inform the decision

Since more phantoms with similar or even equal calibration score may exist, it is important to evaluate the difference between those in terms of principal total strain.

To do that, phantom 12 was considered and compared to the other nineteen. The 6 phantoms that had the calibration score more than 9 (namely, those that varied in x-ray tube current only) were considered and among those slope and intercept coefficients were extracted. Three calibration lines were defined (fig. 3.13) using the highest, average, and lowest couples of *a* and *b* coefficient and eventually used to build three models.

Results from the simulation, evaluated in terms of principal total strain, were compared using mean, standard deviation and variation coefficient.

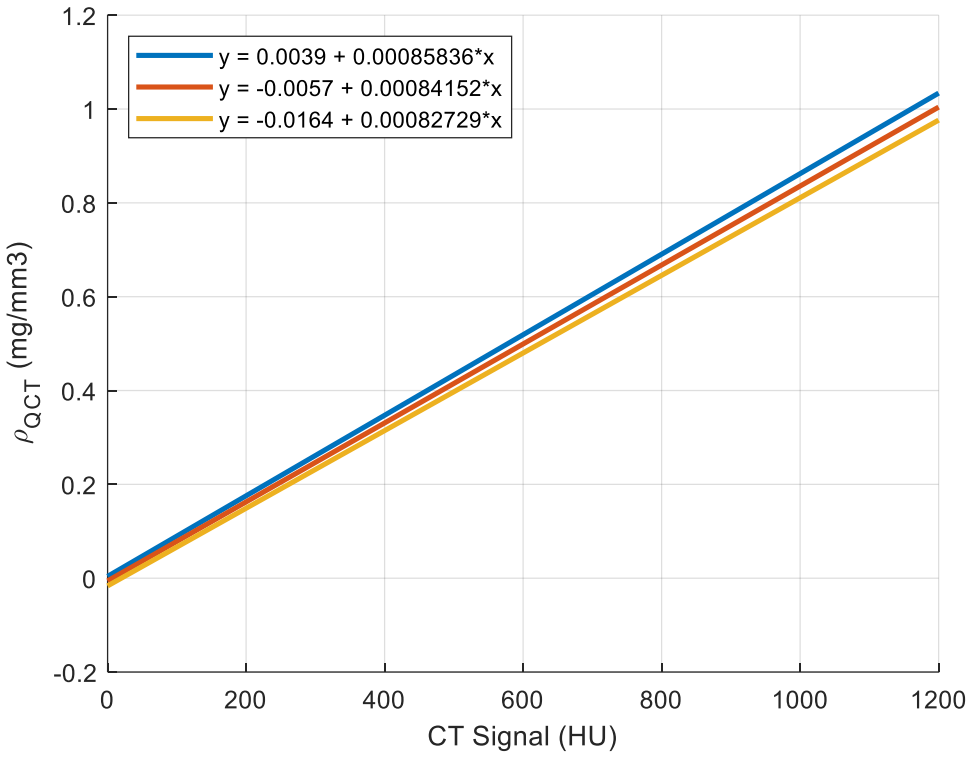

Fig. 3.13 Area of uncertainty defined by the three calibration lines

3.4.4 Uncertainties in Morgan relation

This analysis was conducted to assess the uncertainties related to the Morgan relation, that links the mechanical properties of the bone in term of E with the apparent density. This relation (parametrized in eq. 3.8) is provided along with ninety-five percent confidence interval both for *A* and *B*. *A* is comprised in the range [5440 – 8630] and *B* in the range [1.14 – 1.84].

$$E = A\rho_{app}^{B} \qquad \text{Eq. 3.8}$$

Three equations (eq. 3.9) can thus be obtained using the extreme values of the confidential intervals (fig 3.14).

$$\begin{cases} E = 8630\rho_{app}^{1.84} \\ E = 6850\rho_{app}^{1.49} \\ E = 5440\rho_{app}^{1.14} \end{cases} \qquad \text{Eq. 3.9}$$

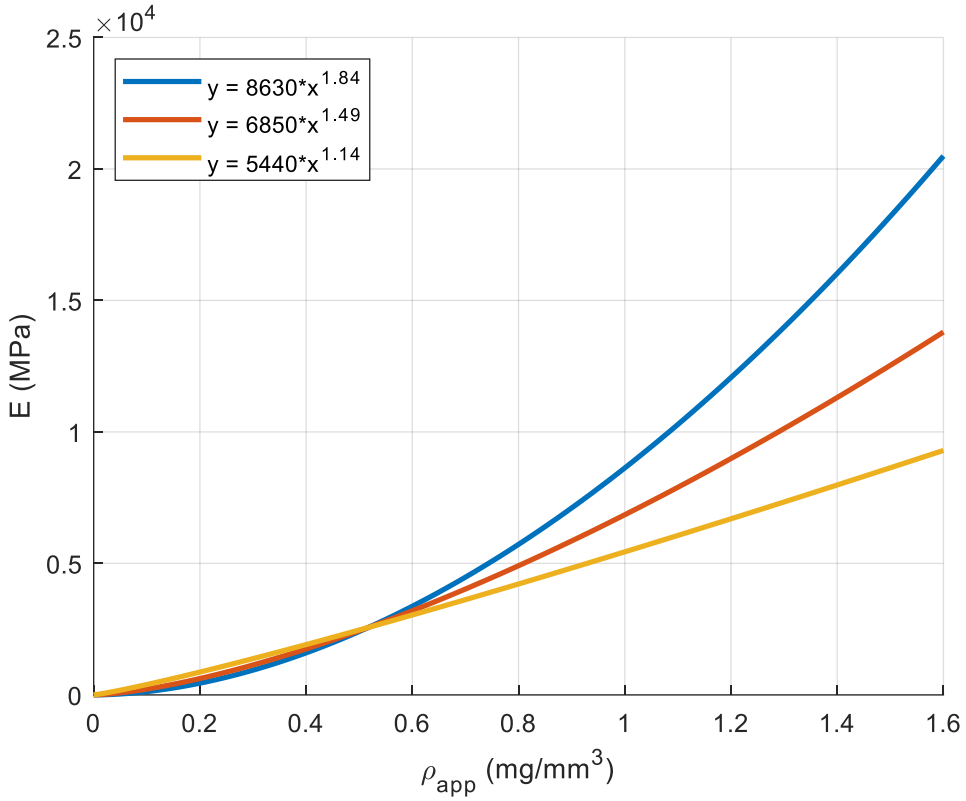

Fig. 3.14 Plot of the three $E - \rho_{app}$ curves

From each equation three models were built and the percentage difference, evaluated in terms of principal total strain, was calculated for the same node with eq. 3.10.

$$d_{\varepsilon}{}^{i} = \left|\frac{\varepsilon^{i*} - \varepsilon^{i}}{\varepsilon^{i*}}\right| \cdot 100 \qquad \text{Eq. 3.10}$$

Superscript *I* refers to models with modified Morgan equation (max or min). The results obtained with the median equation (i^*) were considered as reference solution.

3.5 Effect of uncertainties when defining the BCs

This verification analysis aims to assess the effect of boundary conditions variation (section 2.1.3) on the simulation results. As said before, the QOIs chosen for these analyses is ε. The boundary conditions that could be affected by uncertainties are the position of the cut plane that defines the node selection used in the multi-point constraints approach and the anatomical landmark positions extracted from the virtual palpation step.

3.5.1 Plane for MPC

The cut plane location (section 2.1.3) was varied (fig. 3.15) along the femur shaft identifying three different planes during simulations (eq. 3.11), named respectively mpcBaseN_1, mpcBaseN_2 and mpcBaseN_3 (the one used for the simulations).

$$\begin{cases} mpcBaseN_1 = kneeCenterZ + (femurHeadZ - kneeCenterZ) * 0.75 \\ mpcBaseN_2 = kneeCenterZ + (femurHeadZ - kneeCenterZ) * 0.5 \\ mpcBaseN_3 = kneeCenterZ + (femurHeadZ - kneeCenterZ) * 0.25 \end{cases} \quad \text{Eq. 3.11}$$

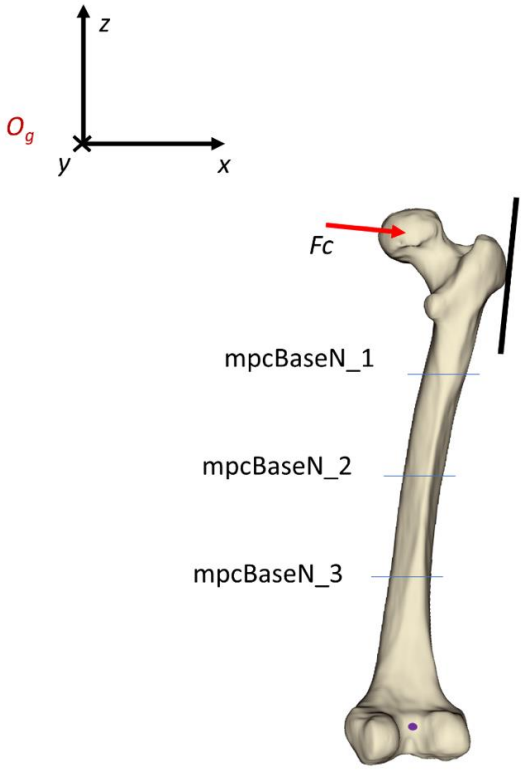

Fig. 3.15 The three planes used for the mpc approach

Percentage errors in ε were calculated with the following relationship (eq. 3.12).

$$e_\varepsilon{}^i = \left|\frac{\varepsilon^{i*} - \varepsilon^i}{\varepsilon^{i*}}\right| \cdot 100 \quad \text{Eq. 3.12}$$

Superscript *i* refers to models with progressively reduced portion of proximal femur over mpc plane. The results obtained with mpcBaseN_3 ($i^* = 3$) were considered as reference solution.

3.5.2 Virtual palpation

As said in section 2.1.3, virtual palpation is a manually conducted operation that consists in identifying ten points (the six extremes of the box containing the femur head, medial and lateral condyle and epicondyle) to define the coordinates of femur

head, head direction, greater trochanter direction and knee center. Since an operator handles this activity, two different types of uncertainties can arise:

- Intra-operator uncertainty
- Inter-operator uncertainty

Intra-operator analysis was conducted doing four different virtual palpations in four different days by the same operator, starting from the same geometry.

Inter-operator analysis was conducted considering four different virtual palpations by four different operators.

Since for this analysis there is no reference value, the uncertainties in input (x, y, z coordinate of femur head, head direction, greater trochanter direction and knee center) and output (maximum principal strain ε) were compared in terms of mean and standard deviation. Also, the variation coefficient in output was calculated (eq. 3.13).

$$CV = \left|\frac{St.Dev}{Mean}\right| \cdot 100 \qquad \text{Eq. 3.13}$$

3.6 Mesh metrics analysis

Mesh metric is an important analysis to assess the degree of quality of the elements. Even if in this pipeline an automatic meshing algorithm is adopted (Octree method), for models with high degrees of freedom mesh-related problems may arise.

Mesh metric was assessed evaluating mean value and standard deviation of five standard parameters in three femurs at 2 mm mesh size, and for the same femur progressively reducing from 2 mm to 0.75 mm. The analyzed parameters, whose values are extracted using Ansys Workbench, were:

- Element quality
- Aspect ratio
- Jacobian ratio
- Maximum corner angle
- Skewness

4 Results and Discussion

4.1 Force and moment equilibrium

Force and Moment equilibrium analysis gave a good agreement and the results obtained are reported in Eq. 4.1 for force and Eq. 4.2 for moment in the three spatial directions:

$$\begin{cases} F_{tot\_x} = -1.94 \cdot 10^{-6} N \\ F_{tot\_y} = -0.026\ N \\ F_{tot\_z} = -2.16 \cdot 10^{-6}\ N \end{cases} \quad \text{Eq. 4.1}$$

$$\begin{cases} M_{tot\_x} = 0.4836\ Nmm \\ M_{tot\_y} = -0.0003\ Nmm \\ M_{tot\_z} = 0.4537\ Nmm \end{cases} \quad \text{Eq. 4.2}$$

Exact results should be zero for three component values of both F_{tot} and M_{tot}. Since differences are very low in module, the discrepancies could be due to approximation errors during the calculations. Indeed:

- the order of magnitude of forces is 10^3, and for the maximum error is 10^{-2}
- the order of magnitude of moments is 10^5, and for the maximum error is 10^{-1}

4.2 Mesh convergence analysis

Mesh convergence analysis results on the maximum principal strain are summed up in tab. 4.1, 4.2 and 4.3. Maximum edge element size, number of DoF, maximum principal strain value, percentage differences and location of node where the results are extracted are reported for the three case studies.

D0062						
MeshSize	DOF	**ε**	**d_ε (%)**	**X (mm)**	**Y (mm)**	**Z (mm)**
4mm	140865	-0.0031	40.40	141.74	-24.76	-120.37
3mm	324969	-0.00332	36.23	141.74	-24.76	-120.37
2mm	1065255	-0.00388	25.49	141.74	-24.76	-120.37
1mm	8360421	-0.00505	2.99	141.74	-24.76	-120.37
0.75mm	19634724	-0.0052	0	141.74	-24.76	-120.37

Tab. 4.1 Mesh convergence of D0062 in ε

L122						
MeshSize	DOF	ε	d_ε (%)	X (mm)	Y (mm)	Z (mm)
4mm	132177	-0.00386	27.31	124.11	-1.75	-119.88
3mm	302715	-0.00394	25.69	124.11	-1.75	-119.88
2mm	992823	-0.00488	8.11	124.11	-1.75	-119.88
1mm	7802310	-0.00502	5.47	124.11	-1.75	-119.88
0.75mm	18296130	-0.00531	0	124.1	-1.75	-119.88

Tab. 4.2 Mesh convergence of L122 in ε

L122						
MeshSize	DOF	ε	d_ε (%)	X (mm)	Y (mm)	Z (mm)
4mm	132177	-0.00414	23.49	115.15	17.11	-168.45
3mm	302715	-0.00445	17.77	115.15	17.11	-168.45
2mm	992823	-0.00505	6.61	115.15	17.11	-168.45
1mm	7802310	-0.00533	1.43	115.15	17.11	-168.45
0.75mm	18296130	-0.00541	0	115.15	17.11	-168.45

Tab. 4.3 Mesh convergence of L123 in ε

Mesh convergence analysis results on the failure load are summed up in tab. 4.4, 4.5 and 4.6. Maximum edge element size, number of DoF, maximum principal strain value, percentage differences and location of node where the results are extracted are reported for the three case studies.

D0062						
MeshSize	DOF	F_Load (N)	d_{FL}(%)	X (mm)	Y (mm)	Z (mm)
4mm	140865	3191.99	3.90	143.51	-31.14	-121.36
3mm	324969	3375.80	9.88	144.64	-27.41	-120.46
2mm	1065255	3205.45	4.34	144.63	-26.25	-120.54
1mm	8360421	3076.55	0.14	143.49	-25.53	-120.55
0.75mm	19634724	3072.01	0	143.88	-25.84	-120.53

Tab. 4.4 Mesh convergence of D0062 in Failure Load

L122						
MeshSize	DOF	F_Load (N)	d_{FL}(%)	X (mm)	Y (mm)	Z (mm)
4mm	132168	2810.58	5.47	123.71	-3.87	-119.76
3mm	302694	3092.51	4	125.12	-7.66	-121.16
2mm	992823	3020.21	1.57	124	-3.74	-119.88
1mm	7772406	3045.27	2.41	124.47	-7.13	-120.49
0.75mm	18296130	2973.50	0	124.72	-7.35	-120.75

Tab. 4.5 Mesh convergence of L122 in Failure Load

L123						
MeshSize	DOF	F_Load (N)	d_{FL}(%)	X (mm)	Y (mm)	Z (mm)
4mm	136047	2002.8	16.58	115.67	19.78	-170.09
3mm	312522	2313.54	3.64	115.67	19.78	-170.09
2mm	1025067	2464.56	2.64	116.15	17.94	-169.27
1mm	8035176	2430	1.20	115.67	19.78	-170.09
0.75mm	18970344	2401.07	0	115.66	19.78	-170.08

Tab. 4.6 Mesh convergence of L123 in Failure Load

The plots of the convergence trends obtained from the two analyses are reported in Fig 4.1.

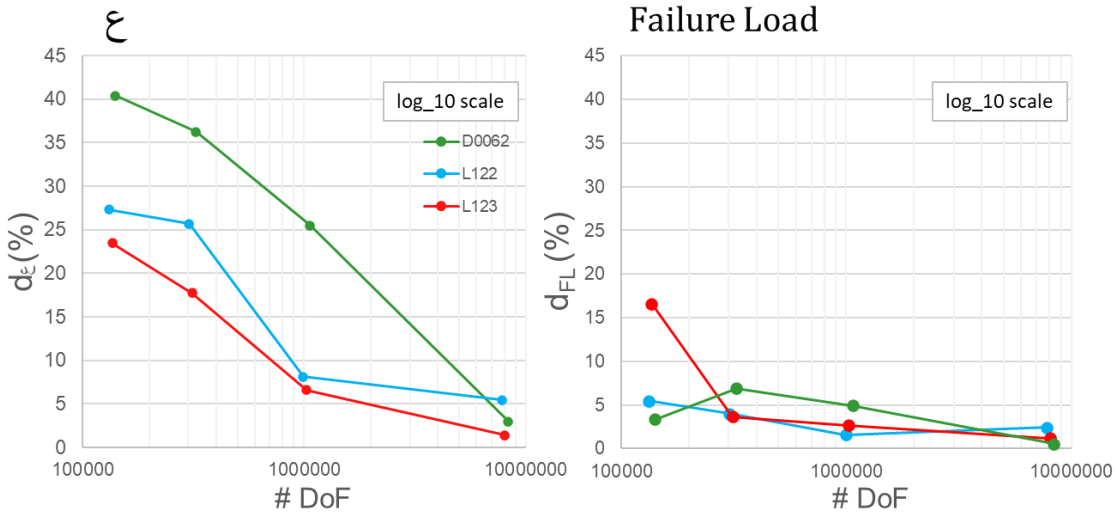

Fig. 4.1 Convergence trends obtained from the two analyses

As also mentioned in Section 3.3.1, in order to assess what is the parameter responsible of the unexpected convergence behavior of D0062, further studies were conducted. Results from SED analysis and Elastic moduli expressed in terms of percentage difference with respect to reference can be found below in fig. 4.2 and 4.3 respectively.

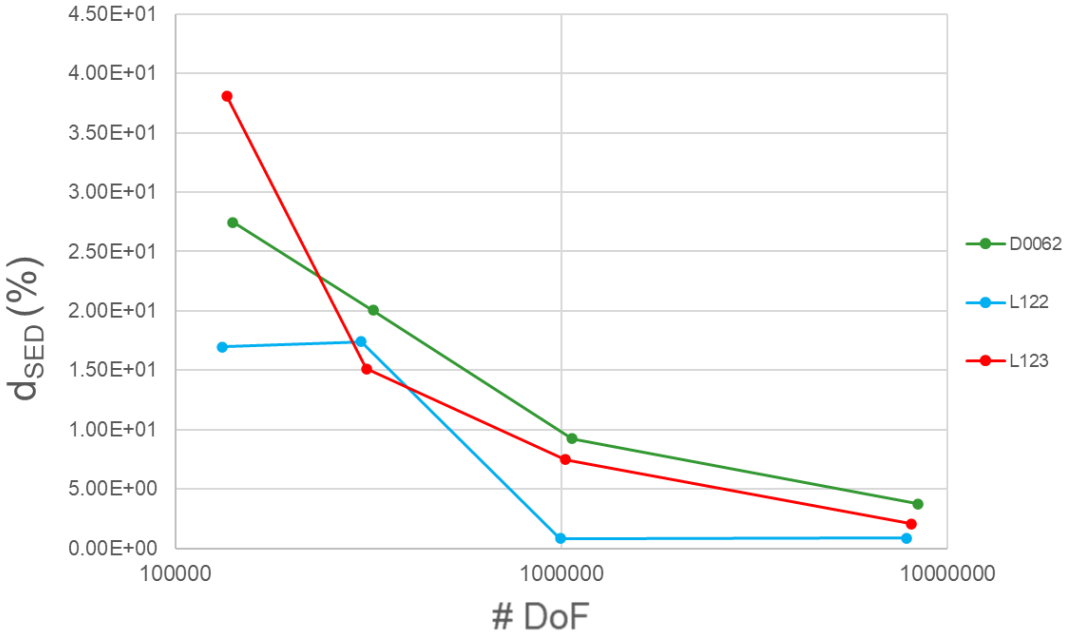

Fig. 4.2 Difference in SED values between D0062 and the other two samples

No evident behaviour can be observed in this graph, since all the femur converged in a similar fashion.

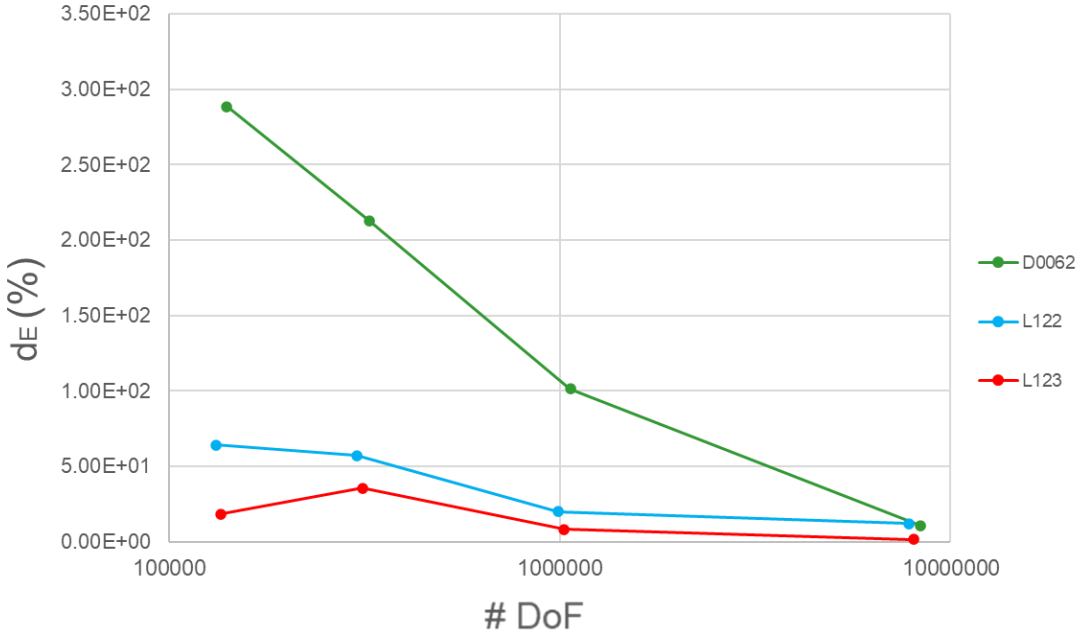

Fig. 4.3 Difference in E values between D0062 and the other two samples

A strong discrepancy can instead be observed in terms of elastic module. In particular, E dropped dramatically in module by reducing element size from 4 mm to 0.75 mm. As said in section 3.3.1, this suggested to redo modified mesh convergence analyses for D0062 patient. The model with the node close to the one with maximum strain is called D0062_bis (tab 4.7), the model with a new geometry from a different segmentation is called D0062_Newsegm (tab. 4.8).

D0062_bis						
MeshSize	DOF	ε	d_ε (%)	X (mm)	Y (mm)	Z (mm)
4mm	140871	-0.0032	19.14	143.88	-25.84	-120.53
3mm	325023	-0.0034	13.79	143.88	-25.84	-120.53
2mm	1065312	-0.0036	7.27	143.88	-25.84	-120.53
1mm	8385894	-0.0041	3.54	143.88	-25.84	-120.53
0.75mm	18970344	-0.0039	0	143.88	-25.84	-120.53

Tab. 4.7 Mesh convergence of D0062_bis

D0062_NewSegm						
MeshSize	DOF	ε	d_ε (%)	X (mm)	Y (mm)	Z (mm)
4mm	140871	-0.0033	31.02	141.80	-24.10	-121.24
3mm	325023	-0.0033	32.54	141.80	-24.10	-121.24
2mm	1065312	-0.0040	17.26	141.80	-24.10	-121.24
1mm	8385894	-0.0043	11.47	141.80	-24.10	-121.24
0.75mm	18970344	-0.0048	0	141.80	-24.10	-121.24

Tab. 4.8 Mesh convergence of D0062_Newsegm

The line chart in fig. 4.4 sums up results from this analysis, plotting percentage difference in principal total strain as a function of the number of degrees of freedom. Data are proposed in $\log_{10}$ scale.

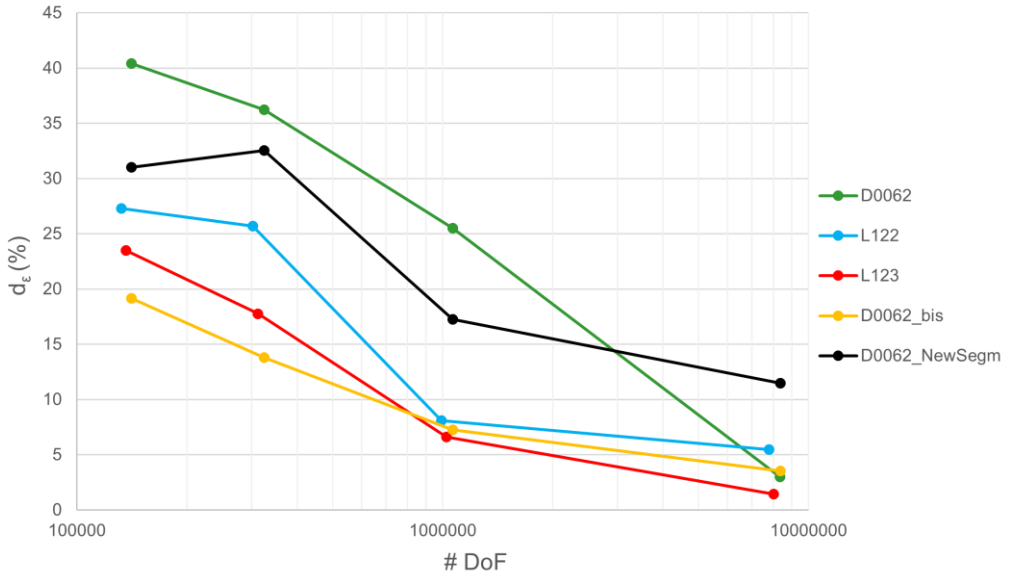

Fig. 4.4 Mesh convergence for the entire cohort of femurs

Since femur D0062 showed a border effect, mesh convergence analysis was evaluated based on the results obtained with the other two femur models, that converged below the threshold of 10% at element size of 2 mm. For this reason, all the subsequent analyses were conducted at element size 2 mm. Femur D0062_bis converged with a comparable behaviour of the other two, D0062_NewSegm showed a better behaviour than D0062, but again no convergence was observed even at 1 mm.

4.3 Uncertainties in material properties mapping

To evaluate uncertainties in material properties mapping four different analyses were conducted. Results of the uncertainties quantification analysis in terms of HU distribution are summed up for full phantom in input in table. 4.9, and in output in table 4.10.

Full phantom - Input				
Regr_line	a $\left(\frac{mg}{mm^3}\right)$	b $\left(\frac{mg}{HUmm^3}\right)$	$d_a(\%)$	$d_b(\%)$
max	0.012	$9.4 \cdot 10^{-4}$	184.6	9.33
med	-0.014	$8.6 \cdot 10^{-4}$		
min	-0.035	$7.9 \cdot 10^{-4}$	154.7	7.89

Tab. 4.9 HU uncertainties propagation in input for the full phantom

Full phantom - Output		
Regr_line	ε	$d_\varepsilon(\%)$
max	$-3.31 \cdot 10^{-3}$	20.22
med	$-4.15 \cdot 10^{-3}$	
min	$-5.06 \cdot 10^{-3}$	22.02

Tab. 4.10 HU uncertainties propagation in output for the full phantom

For the shrinked phantom results are summed up in input in table. 4.11, and in output in table 4.12.

Shrinked phantom - Input				
Regr_line	a $\left(\frac{mg}{mm^3}\right)$	b $\left(\frac{mg}{HUmm^3}\right)$	$d_a(\%)$	$d_b(\%)$
max	0.023	$8.09 \cdot 10^{-4}$	625.4	0.439
med	-0.0044	$8.06 \cdot 10^{-4}$		
min	-0.032	$8.02 \cdot 10^{-4}$	619.8	0.437

Tab. 4.11 HU uncertainties propagation in input for the shrinked phantom

Shrinked phantom - Output		
Regr_line	ε	$d_\varepsilon(\%)$
max	$-3.61 \cdot 10^{-3}$	13.21
med	$-4.16 \cdot 10^{-3}$	
min	$-4.93 \cdot 10^{-3}$	18.28

Tab. 4.12 HU uncertainties propagation in output for the shrinked phantom

This analysis evidenced a great variability using different calibration lines, since one standard deviation error results in a difference up to 22%. However, the main aim of this analysis was to evaluate if the calibration line was sensitive to the HU distribution. Differences in median line, which is the one used to convert HU in ρ_{QCT}, are below 0.5%, thus making the model quite insensitive to variations in HU distribution.

Uncertainties quantification in phantom segmentation are summed up in tab. 4.13 in terms of absolute values and in tab. 4.14 in terms of percentage difference.

	ε
Min	0.0036
Med	0.0032
max	0.0029

Tab. 4.13 Absolute values of principal total strain

	d_{ε}(%)
Min-med	10.83
Med-max	9.042

Tab. 4.14 Percentage difference in principal total strain

This analysis evidenced an important variability using different phantom segmentations, since one standard deviation error results in a difference up to 11%. This suggests that the model is sensitive to phantom segmentation.

Uncertainties quantification in phantom choice are summed up in tab. 4.15 in terms of absolute values of principal total strain and in tab. 4.16 in terms of mean, standard deviation and variation coefficient.

	ε
min	0.0034
med	0.0031
max	0.0029

Tab. 4.15 Absolute values of principal total strain

	ε
Mean	0.0031
St.Dev	0.00023
C.V. %	7.25

Tab. 4.16 Percentage difference in principal total strain

This analysis evidenced a medium variability using different phantom, since one standard deviation error results in a difference up to 7.5%. This suggests that the model is sensitive to phantom choice.

The uncertainties in Morgan relation are summed up in terms of absolute values in tab. 4.17 and in percentage difference in table 4.18.

Morgan Relation	ε
$Eq.1$	-0.0042
$Eq.2$	-0.0041
$Eq.3$	-0.0039

Tab. 4.17 Absolute values of principal total strain

Morgan Relation	$d_{\varepsilon}(\%)$
$Eq.1-2$	2.78
$Eq.2-3$	5.13

Tab. 4.18 Percentage difference in principal total strain

This analysis evidenced a low variability using different density-elasticity relationships, since an error of two standard deviation results in a difference up to 5.5%. This suggests that the model is low sensitive to density-elasticity relationship.

4.4 Effect of uncertainties when defining the BCs

Results of the mpc dependence analysis are summarized in table 4.19 below.

cut plane for mpc	ε	$e_{\varepsilon}(\%)$
$mpcBaseN_1$	-0.00402	0.42
$mpcBaseN_2$	-0.00401	0.28

Tab. 4.19 Effect of uncertainties in cut plane for mpc definition

Since difference are all below 0.5%, the quantity of interest is considered almost insensitive to the position of the cut plane that defines mpc.

In Virtual palpation analysis, results for Intra-operator uncertainty quantification are summed up in table. 4.20 in input, and in table 4.21 in output.

QOIs	Mean (mm)	St.Dev (mm)
femurHeadX	114.655	0.099
femurHeadY	-32.556	0.034
femurHeadZ	-114.850	0.062
headDirX	117.232	0.107
headDirY	-35.056	0.0379
headDirZ	-89.554	0.080
greatTrochX	166.834	0.877
greatTrochY	-39.963	0.133
greatTrochZ	-114.835	0.477
kneeCenterX	75.994	0.120
kneeCenterY	4.936	0.457
kneeCenterZ	-494.279	0.375

Tab. 4.20 Intra-operator uncertainties propagation in input

	ε
Mean	0.0031
St.Dev	$8.63 \cdot 10^{-7}$
C.V. %	0.027

Tab. 4.21 Intra-operator uncertainties propagation in output

Results for Inter-operator uncertainty quantification analysis are summed up in table. 4.22 in input, and in table 4.23 in output.

QOIs	Mean (mm)	St.Dev (mm)
femurHeadX	114.810	0.194
femurHeadY	-32.861	0.679
femurHeadZ	-114.713	0.211
headDirX	117.387	0.197
headDirY	-35.447	0.740
headDirZ	-89.450	0.239
greatTrochX	164.600	3.744
greatTrochY	-40.093	0.940
greatTrochZ	-115.147	0.184
kneeCenterX	76.154	0.347
kneeCenterY	5.926	1.260
kneeCenterZ	-493.660	0.981

Tab. 4.22 Inter-operator uncertainties propagation in input

	ε
Mean	0.0031
St.Dev	$4.71 \cdot 10^{-5}$
C.V. %	1.48

Tab. 4.23 Inter-operator uncertainties propagation in output

Virtual palpation analysis showed that inter operator uncertainties are higher than the intra ones, and that in general they do not significantly affect results in the quantity of interest, since the percentage variation coefficient (C.V.) is always below 1.5%.

4.5 Mesh Metric analysis

Mesh metrics analysis results are summed up in tab. 4.24 and fig. 4.5.

D0062						
		Element Quality	Aspect Ratio	Jacobian Ratio	Maximum Corner	Skewness Mesh
	min	0.41	1.18	1	71.66°	$2.09 \cdot 10^{-4}$
	max	0.99	4.74	1	140.88°	$6.00 \cdot 10^{-1}$
	mean	0.90	1.63	1	91.52°	$1.06 \cdot 10^{-1}$
2mm	StDev	$6.14 \cdot 10^{-2}$	0.22	0	5.65°	$8.90 \cdot 10^{-1}$
L121						
		Element Quality	Aspect Ratio	Jacobian Ratio	Maximum Corner	Skewness Mesh
	min	0.42	1.17	1	71.64°	$1.12 \cdot 10^{-3}$
	max	0.99	4.85	1.0003	142.05°	$6.00 \cdot 10^{-1}$
	mean	0.90	1.63	1	91.67°	$1.10 \cdot 10^{-1}$
2mm	StDev	$6.40 \cdot 10^{-2}$	0.23	$4.59 \cdot 10^{-5}$	5.87°	$9.24 \cdot 10^{-2}$
L122						
		Element Quality	Aspect Ratio	Jacobian Ratio	Maximum Corner	Skewness Mesh
	min	0.40	1.17	1	71.52°	$2.20 \cdot 10^{-3}$
	max	0.99	5.04	1.0003	143.39°	$6.00 \cdot 10^{-1}$
	mean	0.90	1.63	1	91.58°	$1.08 \cdot 10^{-1}$
2mm	StDev	$6.28 \cdot 10^{-2}$	0.23	$4.89 \cdot 10^{-5}$	5.79°	$9.09 \cdot 10^{-2}$

Tab. 4.24 Mean and standard deviation of the mesh metric quantities

According to (Burkhart et al., 2013) acceptable values for mesh metric analysis are:

- ***Aspect Ratio**:* For tethraedral element, percentage of elements with Aspect Ratio over 3 should be less than 5%
- ***Angle Idealization:*** For tethraedral element, angle should be included in range 30°-150°.
- ***Jacobian (MAPDL):*** Jacobian ratio should be near to 1 as much as possible. The more is fair the more mid-side nodes are close to the centre of element.
- ***Skewness***: Skewness values are tabulated in tab. 4.25. Values under 0.25 are considered excellent.

Value of Skewness	Cell Quality
1	Degenerate
0.9 - <1	Bad (sliver)
0.75 – 0.9	Poor
0.5 – 0.75	Fair
0.25 – 0.5	Good
>0 – 0.25	Excellent
0	Equilateral

Tab. 4.25 Range of skewness value

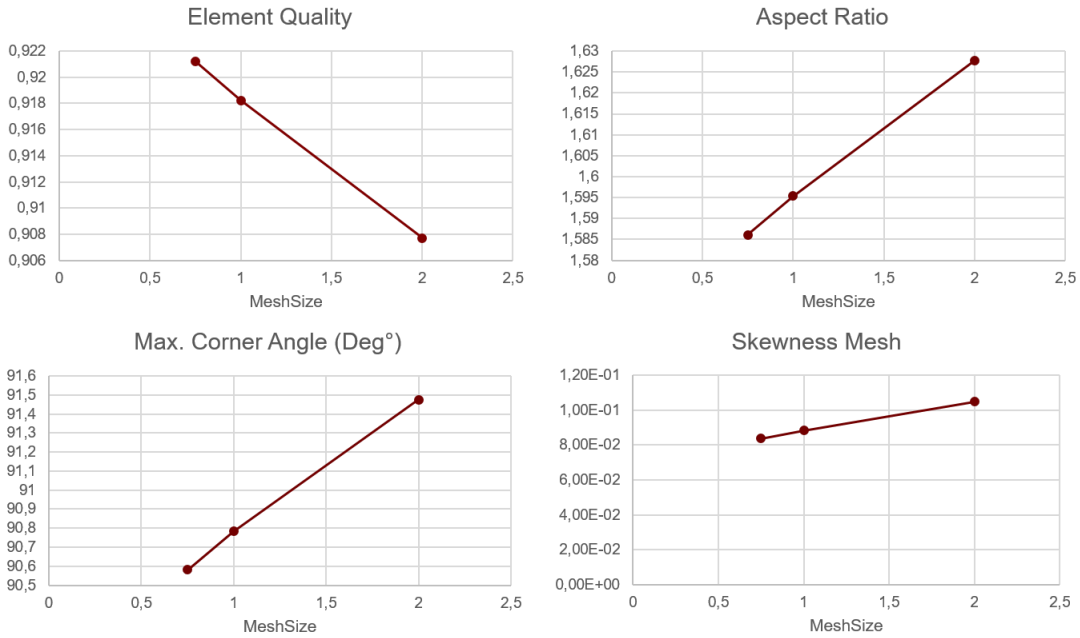

Fig. 4.5 Mesh metric reducing from 2 to 0.75 mm

In our case, percentage of elements with Aspect Ratio over 3 is 0.15%, angle idealization is 90°, Jacobian is equal to 1 and skewness mean is 0.108. Also mesh metric parameters improved as element size reduced. As expected mesh metrics results are excellent since we used an automatic meshing algorithm.

5 Conclusions

In this study, important verification and uncertainty quantification analyses on the BBCT methodology were conducted following the risk-based credibility assessment framework recently proposed in the VV-40 standard by the American Society of Mechanical Engineers (ASME V&V-40 2018). The analyses focused on the main verification tests used in computational solid mechanics: force and moment equilibrium check, mesh convergence analysis, uncertainties evaluation in boundary conditions and material properties mapping, and quality mesh metric study.

Results of these analyses showed that the mathematical model is rightly implemented. The operation that mostly affect the model results is the material properties mapping step.

This work represents an important step that, together with the ongoing clinical validation activities, will contribute to demonstrate the credibility of the BBCT methodology. The VV&UQ plan will be soon submitted as evidence for qualification of the method to a regulatory authority.

Bibliography

3D Slicer image computing platform | 3D Slicer [WWW Document], n.d. URL https://www.slicer.org/ (accessed 11.19.21).

Aldieri, A., Terzini, M., Osella, G., Priola, A.M., Angeli, A., Veltri, A., Audenino, A.L., Bignardi, C., 2018. Osteoporotic Hip Fracture Prediction: Is T-Score-Based Criterion Enough? A Hip Structural Analysis-Based Model. Journal of Biomechanical Engineering 140, 111004. https://doi.org/10.1115/1.4040586

Altai, Z., Qasim, M., Li, X., Viceconti, M., 2019. The effect of boundary and loading conditions on patient classification using finite element predicted risk of fracture. Clinical Biomechanics 68, 137–143. https://doi.org/10.1016/j.clinbiomech.2019.06.004

Amin, S., Kopperdhal, D.L., Melton, L.J., Achenbach, S.J., Therneau, T.M., Riggs, B.L., Keaveny, T.M., Khosla, S., 2011. Association of hip strength estimates by finite-element analysis with fractures in women and men. J Bone Miner Res 26, 1593–1600. https://doi.org/10.1002/jbmr.347

Apple, D.J., Hayes, W., 1993. Prevention of Falls and Hip Fractures in the Elderly. American Academy of Orthopedic Surgeons, Rosemont (IL).

ASME, 2018. Assessing credibility of computational modelling through verification and validation: application to medical devices.

Baumgaertner, M.R., Curtin, S.L., Lindskog, D.M., Keggi, J.M., 1995. The value of the tip-apex distance in predicting failure of fixation of peritrochanteric fractures of the hip. J Bone Joint Surg Am 77, 1058–1064. https://doi.org/10.2106/00004623-199507000-00012

Bhattacharya, P., Altai, Z., Qasim, M., Viceconti, M., 2019. A multiscale model to predict current absolute risk of femoral fracture in a postmenopausal population. Biomech Model Mechanobiol 18, 301–318. https://doi.org/10.1007/s10237-018-1081-0

Burkhart, T.A., Andrews, D.M., Dunning, C.E., 2013. Finite element modeling mesh quality, energy balance and validation methods: A review with recommendations associated with the modeling of bone tissue. Journal of Biomechanics 46, 1477–1488. https://doi.org/10.1016/j.jbiomech.2013.03.022

CFR - Code of Federal Regulations Title 21 [WWW Document], n.d. URL https://www.accessdata.fda.gov/scripts/cdrh/cfdocs/cfcfr/cfrsearch.cfm?fr=820.3 (accessed 4.7.21).

Dharia, M.A., Snyder, S., Bischoff, J.E., 2020. Computational Model Validation of Contact Mechanics in Total Ankle Arthroplasty. J. Orthop. Res. 38, 1063–1069. https://doi.org/10.1002/jor.24551

Driscoll, P., 2006. Gray's Anatomy, 39th Edition. Emerg Med J 23, 492. https://doi.org/10.1136/emj.2005.027847

Endo, Y., Aharonoff, G.B., Zuckerman, J.D., Egol, K.A., Koval, K.J., 2005. Gender differences in patients with hip fracture: a greater risk of morbidity and mortality in men. J Orthop Trauma 19, 29–35. https://doi.org/10.1097/00005131-200501000-00006

Enns-Bray, W.S., Bahaloo, H., Fleps, I., Pauchard, Y., Taghizadeh, E., Sigurdsson, S., Aspelund, T., Büchler, P., Harris, T., Gudnason, V., Ferguson, S.J., Pálsson, H., Helgason, B., 2019. Biofidelic finite element models for

accurately classifying hip fracture in a retrospective clinical study of elderly women from the AGES Reykjavik cohort. Bone 120, 25–37. https://doi.org/10.1016/j.bone.2018.09.014
Gennari, C., Avioli, L.V., 1991. Atlante delle malattie dell'osso. Osteofix Library.
International Osteoporosis Foundation | IOF [WWW Document], n.d. URL https://www.osteoporosis.foundation/ (accessed 11.11.21).
Jetté, B., Brailovski, V., Dumas, M., Simoneau, C., Terriault, P., 2018. Femoral stem incorporating a diamond cubic lattice structure: Design, manufacture and testing. Journal of the Mechanical Behavior of Biomedical Materials 77, 58–72. https://doi.org/10.1016/j.jmbbm.2017.08.034
Koval, null, Zuckerman, null, 1994. Hip Fractures: I. Overview and Evaluation and Treatment of Femoral-Neck Fractures. J Am Acad Orthop Surg 2, 141–149. https://doi.org/10.5435/00124635-199405000-00002
Löfman, O., Berglund, K., Larsson, L., Toss, G., 2002. Changes in hip fracture epidemiology: redistribution between ages, genders and fracture types. Osteoporos Int 13, 18–25. https://doi.org/10.1007/s198-002-8333-x
Mimics, n.d. . Materialise, Leuven, Belgium.
Montgomery, D., 2017. Design and Analysis of Experiments, 2017th ed.
Morgan, E.F., Bayraktar, H.H., Keaveny, T.M., 2003. Trabecular bone modulus–density relationships depend on anatomic site. Journal of Biomechanics 36, 897–904. https://doi.org/10.1016/S0021-9290(03)00071-X
Orwoll, E.S., Marshall, L.M., Nielson, C.M., Cummings, S.R., Lapidus, J., Cauley, J.A., Ensrud, K., Lane, N., Hoffmann, P.R., Kopperdahl, D.L., Keaveny, T.M., for the Osteoporotic Fractures in Men (MrOS) Study Group, 2009. Finite Element Analysis of the Proximal Femur and Hip Fracture Risk in Older Men. Journal of Bone and Mineral Research 24, 475–483. https://doi.org/10.1359/jbmr.081201
Qasim, M., Farinella, G., Zhang, J., Li, X., Yang, L., Eastell, R., Viceconti, M., 2016. Patient-specific finite element estimated femur strength as a predictor of the risk of hip fracture: the effect of methodological determinants. Osteoporos Int 27, 2815–2822. https://doi.org/10.1007/s00198-016-3597-4
Schileo, E., Dall'Ara, E., Taddei, F., Malandrino, A., Schotkamp, T., Baleani, M., Viceconti, M., 2008. An accurate estimation of bone density improves the accuracy of subject-specific finite element models. Journal of Biomechanics 41, 2483–2491. https://doi.org/10.1016/j.jbiomech.2008.05.017
Schrøder, H.M., Petersen, K.K., Erlandsen, M., 1993. Occurrence and incidence of the second hip fracture. Clin Orthop Relat Res 166–169.
Sternheim, A., Giladi, O., Gortzak, Y., Drexler, M., Salai, M., Trabelsi, N., Milgrom, C., Yosibash, Z., 2018. Pathological fracture risk assessment in patients with femoral metastases using CT-based finite element methods. A retrospective clinical study. Bone 110, 215–220. https://doi.org/10.1016/j.bone.2018.02.011
Wanki, G., Ekwaro-Osire, S., Dias, J.P., Cunha, A., 2020. Uncertainty Quantification With Sparsely Characterized Parameters: An Example Applied to Femoral Stem Mechanics. Journal of Verification, Validation and Uncertainty Quantification 5, 031005. https://doi.org/10.1115/1.4048749
Yosibash, Z., Padan, R., Joskowicz, L., Milgrom, C., 2007. A CT-Based High-Order Finite Element Analysis of the Human Proximal Femur Compared to In-vitro

Experiments. Journal of Biomechanical Engineering 129, 297–309. https://doi.org/10.1115/1.2720906
Zienkiewicz, O.C., Taylor, R.L., Zhu, J.Z., 2005. The Finite Element Method: Its Basis and Fundamentals - 6th Edition [WWW Document]. URL https://www.elsevier.com/books/the-finite-element-method-its-basis-and-fundamentals/zienkiewicz/978-0-08-047277-5 (accessed 11.22.21).